



**HAL**  
open science

# A global palaeoclimatic reconstruction for the Valanginian based on clay mineralogical and geochemical data

Guillaume Charbonnier, Stéphanie Duchamp-Alphonse, Jean-François Deconinck, Thierry Adate, Jorge Spangenberg, Christophe Colin, Karl Föllmi

► **To cite this version:**

Guillaume Charbonnier, Stéphanie Duchamp-Alphonse, Jean-François Deconinck, Thierry Adate, Jorge Spangenberg, et al.. A global palaeoclimatic reconstruction for the Valanginian based on clay mineralogical and geochemical data. *Earth-Science Reviews*, 2020, 202, pp.103092. 10.1016/j.earscirev.2020.103092 . hal-02448620

**HAL Id: hal-02448620**

**<https://hal.science/hal-02448620v1>**

Submitted on 19 Jul 2024

**HAL** is a multi-disciplinary open access archive for the deposit and dissemination of scientific research documents, whether they are published or not. The documents may come from teaching and research institutions in France or abroad, or from public or private research centers.

L'archive ouverte pluridisciplinaire **HAL**, est destinée au dépôt et à la diffusion de documents scientifiques de niveau recherche, publiés ou non, émanant des établissements d'enseignement et de recherche français ou étrangers, des laboratoires publics ou privés.

1 **A global palaeoclimatic reconstruction for the Valanginian based on clay mineralogical and**  
2 **geochemical data**

3  
4 Guillaume Charbonnier<sup>1-2\*</sup>, Stéphanie Duchamp-Alphonse<sup>2</sup>, Jean-François Deconinck<sup>3</sup>, Thierry  
5 Adatte<sup>1</sup>, Jorge E. Spangenberg<sup>4</sup>, Christophe Colin<sup>2</sup>, Karl B. Föllmi<sup>1</sup>

6  
7 1. Institute of Earth Sciences, University of Lausanne, Géopolis, CH-1015 Lausanne, Switzerland

8 2. UMR CNRS 8148 GEOPS, Université Paris Sud XI, Bâtiment 504, 91405 Orsay, France.

9 3. UMR CNRS 6282 Biogéosciences Université de Bourgogne/Franche-Comté, 6 Bd. Gabriel,  
10 21000 Dijon, France.

11 4. Institute of Earth Surface Dynamics, University of Lausanne, Géopolis, CH-1015 Lausanne,  
12 Switzerland.

13  
14 \* Corresponding author.

15 *E-mail address:* guillaume.charbonnier@unil.ch (G. Charbonnier)

16 Telephone number: 00 41 (0) 21 692 43 10

17  
18  
19  
20  
21  
22  
23  
24  
25  
26

27 **Abstract**

28

29 High-resolution clay mineral and  $\delta^{18}\text{O}_{\text{carb}}$  analyses have been performed on three sections of  
30 Valanginian age (Early Cretaceous), from northwestern ( $\sim 20\text{--}30^\circ\text{N}$ ) and southern ( $\sim 53^\circ\text{S}$ ) Tethyan  
31 realms. The data have been integrated in a large set of published mineralogical (clays), and  
32 geochemical ( $\delta^{18}\text{O}_{\text{carb}}$ ,  $\delta^{18}\text{O}_{\text{bivalve}}$ ,  $\delta^{18}\text{O}_{\text{lenticulina}}$ ,  $\delta^{18}\text{O}_{\text{belemnite}}$ , and  $\text{TEX}_{86}$ ) data from 17 sections,  
33 situated between  $\sim 45^\circ\text{N}$  and  $\sim 53^\circ\text{S}$ . Based on this data set, we provide new insights into  
34 Valanginian climate conditions from a wide range of palaeolatitudes. We highlight climate trends  
35 within specific areas and identify main climate belts. In the Proto-North Atlantic realm ( $\sim 15\text{--}17^\circ\text{N}$ )  
36 large amounts of smectite together with the occurrence of palygorskite testify for a semi-arid  
37 climate belt throughout the Valanginian. Significant variations in kaolinite content in the  
38 northwestern Tethyan realm ( $\sim 20$  to  $30^\circ\text{N}$ ) suggest that this realm has been more sensitive to  
39 changes in hydrological cycling and subsequent erosion and runoff processes during the early to  
40 early-late Valanginian transition interval. This time interval, that is coincident with the pronounced  
41 positive and globally recognized carbon isotope excursion (CIE; the Weissert episode), documents  
42 the wet conditions of a humid subtropical climate belt. Temperature ranges derived from  $\delta^{18}\text{O}$   
43 records suggest climate warming by about  $3\text{--}5\pm 0.9^\circ\text{C}$  in the northern hemisphere, during the  
44 Weissert episode. This is followed by a global cooling of about ca.  $1\text{--}5\pm 0.9^\circ\text{C}$  in both hemispheres,  
45 during the late Valanginian.

46 We postulate that these patterns were due to interplays between tectonic and orbital factors,  
47 which have controlled the distribution of regional palaeoclimate belts during the Valanginian. The  
48 semi-arid belt expressed in the Proto North Atlantic realm has probably been induced by its specific  
49 palaeogeographic configuration and the existence of isolated basins, which were each characterized  
50 by strong and continuous thermohaline circulation. An eccentricity paced monsoon-like system  
51 might have played a significant role in maintaining the subtropical belt around the northwestern  
52 Tethyan realm, up to the mid latitudes ( $\sim 35\text{--}45^\circ\text{N}$ ). Superimposed on these regional processes, a

53 widespread magmatic pulse in Paraná-Etendeka volcanic activity might have stimulated greenhouse  
54 conditions, impacting marine biota and favouring the development of a dense vegetation cover on  
55 the continent. An increase in sedimentary burial of  $^{13}\text{C}$  depleted organic carbon on the continents  
56 may have contributed to the progressive global positive carbon isotope excursion. In the medium  
57 term, it has also probably led to a significant decrease in atmospheric  $\text{CO}_2$ , as testified by the global  
58 cooling recorded during the late Valanginian in both hemispheres and the probable concomitant  
59 extension of polar ice caps.

60

61 *Keywords:* hydrolysing conditions; temperature range; palaeoclimate belt; volcanic activity; global  
62 reconstruction; Valanginian.

63

## 64 **1. Introduction**

65

66 Historically, the Cretaceous ( $145\pm 0.8$ – $66\pm 0.05$  Ma; Ogg et al., 2016) has been referred to a  
67 period of greenhouse Earth, characterized by warm and equal conditions (e.g., Hallam, 1985; Frakes  
68 et al., 1992). However, in the last decades, numerous studies have documented evidences for the  
69 existence of shorter episodes of considerable palaeoclimatic and palaeoenvironmental changes (e.g.,  
70 Jenkyns, 2010; Föllmi, 2012). The Valanginian time interval represents such a dynamic phase. In  
71 sedimentary archives, important changes in the global carbon cycle are expressed by a significant  
72 positive carbon isotope excursion (CIE) at the early–late Valanginian transition, known as the  
73 “Weissert episode” (e.g., Cotillon and Rio, 1984; Weissert, 1989; Erba et al., 2004; Bornemann and  
74 Mutterlose, 2008; Charbonnier et al., 2013). The CIE is preceded by and associated with several  
75 phases of carbonate platform drowning (Schlager, 1989; Föllmi et al., 1994, 2006; Graziano, 1999),  
76 as well as with widespread turnovers (from oligotrophic to mesotrophic assemblages) and crises in  
77 pelagic (planktonic and benthic organisms) and neritic (bioconstructions) carbonate biota (Channell  
78 et al., 1993; Erba and Tremolada, 2004; Duchamp-Alphonse et al., 2007, 2014; Barbarin et al.,

79 2012). Numerous indicators of cooler conditions such as glendonites, dropstones, tillite deposits and  
80 ice rafted debris, have been recognized in Valanginian sediments in Australian, Canadian,  
81 Spitsbergen, and Siberian basins (e.g. Kemper and Schmitz, 1975; Price, 1999; Alley and Frakes,  
82 2003; Price and Nunn, 2010; Alley et al., 2019; Vickers et al., 2019). Furthermore, changes in  
83 calcareous nannofossil assemblages (Melinte and Mutterlose, 2001), oxygen isotope data (Van de  
84 Schootbrugge et al., 2000; Pucéat et al., 2005; McArthur et al., 2007; Barbarin et al., 2012;  
85 Meissner et al., 2015) and more recently, Mg/Ca measurements (Price et al., 2018), have evidenced  
86 an overall 2 to 4°C cooling trend within the northern hemisphere during the late Valanginian, which  
87 may suggest the presence of a polar ice cap (McArthur et al., 2007; Price and Passey, 2013). In  
88 parallel, clay mineral records from the northwestern Tethys have highlighted short-term  
89 Valanginian palaeoclimate fluctuations in low to mid latitudes, with warm and humid conditions  
90 during the Weissert episode, and drier conditions during the cooler phase in the late Valanginian  
91 (Duchamp-Alphonse et al., 2011; Westermann et al., 2013; Charbonnier et al., 2016). An important  
92 magmatic pulse related to the volcanic activity of the Parana-Etendeka traps has been postulated to  
93 have triggered the Valanginian environmental perturbations (Föllmi et al., 1994; Erba et al., 2004;  
94 Martinez et al., 2015; Charbonnier et al., 2017). Massive volcanism and the associated released of  
95 CO<sub>2</sub> in the ocean-atmosphere system may have accelerated the hydrological cycle, intensified  
96 silicate weathering, and fertilized the coastal environments; thereby affecting both marine and  
97 terrestrial ecosystems (Föllmi et al., 1994; Erba et al., 2004; Charbonnier et al., 2017).

98         While such results may provide a rather clear image of the evolution of climate during the  
99 Valanginian, new and contrasting findings have challenged this particular view, rendering the  
100 reconstructions of palaeoclimate conditions that prevailed during the Valanginian more elusive. The  
101 most striking controversial examples are the TEX<sub>86</sub> records from the Proto North Atlantic (~15–  
102 17°N) and the southern Tethyan (~53°S) realms, which document high and rather stable sea-surface  
103 temperatures (SST of ~33 to 34°C and ~26°C, respectively) through the entire Valanginian (Littler  
104 et al., 2011). As a consequence, these authors have re-evaluated the earliest Cretaceous as a warm

105 and stable period. In addition, recent petrological and geochemical analyses on the complex  
106 sequence of ikaite-calcite precipitation leading to glendonite formation suggest that glendonites  
107 document past events of methane release and oxidation in polar settings rather than cold-water  
108 conditions (e.g., Morales et al., 2017). Similarly, the origin of dropstones in the geological record  
109 can be related to non-glacial mechanisms such as gravity processes or wood rafting, implying that  
110 these deposits cannot consistently be interpreted as the result of ice rafting and therefore cool  
111 climate (Bennett et al., 1994, 1996; Doublet and Garcia, 2004).

112 This controversy in the interpretation of climate evolution during the Valanginian is  
113 promoted by the lack of high-resolution climate reconstructions in the southern hemisphere based  
114 on geochemistry and clay mineralogy (Ditchfield, 1997; Price and Nunn, 2010; Littler et al., 2011;  
115 Price and Passey, 2013). Here, we provide new insights into Valanginian climate conditions from a  
116 wide range of palaeolatitudes, in order to highlight main trends within specific realms, and  
117 emphasize the presence and localization of main climate belts. This study is based upon new clay  
118 mineral and  $\delta^{18}\text{O}_{\text{carb}}$  data from the northwestern ( $\sim 20\text{--}30^\circ\text{N}$ ) and southern ( $\sim 53^\circ\text{S}$ ) Tethys realms.  
119 These data have been integrated into a set of published clay,  $\delta^{13}\text{C}$ ,  $\delta^{18}\text{O}$ , and  $\text{TEX}_{86}$  data from sites  
120 situated between  $\sim 45^\circ\text{N}$  and  $\sim 53^\circ\text{S}$  (Table 1, Fig. 1). Our multiproxy approach helps specifying  
121 weathering intensity on continents and documenting humid and arid climate belts. It is also useful to  
122 re-evaluate previous geochemical results and propose coherent palaeotemperature patterns on a  
123 global scale.

124

## 125 **2. Data compilation and method**

126

127 Published and unpublished geochemical and mineralogical data from the Valanginian have  
128 been compiled within a sizeable database presented in Tables 1A and B. In detail, 1924 oxygen  
129 isotope measurements represented by  $\delta^{18}\text{O}$  values of whole-rock carbonate ( $\delta^{18}\text{O}_{\text{carb}}$ ), hand-picked  
130 benthic foraminifera ( $\delta^{18}\text{O}_{\text{lent}}$ : *Lenticulina* spp.), bivalves ( $\delta^{18}\text{O}_{\text{biv}}$ ), and belemnite samples ( $\delta^{18}\text{O}_{\text{bel}}$ ),

131 37 TEX<sub>86</sub> analyses, as well as 257 clay mineral data, have been gathered from 17 reference sections.  
132 These published data have been complemented by 69 new geochemical and 347 new mineralogical  
133 analyses on three reference sections, situated in the northwestern (Barranco del Garranchal and  
134 Molinas de las Oicas sections, Betic cordillera, south-east Spain) and the southern (ODP Site 765C)  
135 Tethyan realms (Fig. 1). Lithological, palaeogeographical and depositional settings of the selected  
136 sections are given in Table 1. These sections are located in the southern part of the Boreal (~35–  
137 45°N), the northwestern (~20–30°N) and southern (~53°S) Tethyan, and the Proto North Atlantic  
138 (~15–17°N) realms (Table 1 and Fig. 1). They all benefit from robust biostratigraphic and/or  
139 magnetostratigraphic constraints as well as detailed carbon-isotope stratigraphies, which provide a  
140 most useful tool for regional to global correlations given their characteristic evolution (Wendler,  
141 2013).

142 The composition of clay mineral assemblages selected in the database has been analyzed by  
143 XRD method on the <2 µm clay fraction of sediments using the classical analytic procedure  
144 described by Moore and Reynolds (1997). Kaolinite, illite, chlorite, palygorskite, smectite, and  
145 illite/smectite irregular mixed-layers (R0) were identified in the sections. The R0 I-S minerals,  
146 which contain more than 60 % of smectite layers, have been included in the smectite group and will  
147 hereafter be called “smectite”. Oxygen and carbon stable isotope data selected here have been  
148 obtained using isotope ratio mass spectrometry and reported in the delta notation ( $\delta$ ) as the per mil  
149 (‰) deviation relative to the Vienna Pee Dee Belemnite standard (VPDB). Detailed methodologies  
150 have been described in the Supplementary Online Materials (SOM). These data have been obtained  
151 from various laboratories using different instruments and standards, which may introduce possible  
152 bias for a global compilation (see Table S1 in Supplementary Online Materials). Therefore, in order  
153 to maximize the applicability of the data, LOESS smoothing curves (i.e. locally weighted scatterplot  
154 smoothing, Cleveland and Devlin, 1988), have been used for the mineralogical and geochemical  
155 datasets, for each highlighted realm (Table 1 and Figs. 2–5). Within their 95 % confidence levels  
156 (statistical precision of 5 %,  $2\sigma$ ; Figs. 2-5), they have the potential to highlight main regional

157 palaeoenvironmental trends.

158

### 159 **3. Results**

160

#### 161 3.1. Northern hemisphere data

162

##### 163 3.1.1. Northwestern Tethyan realm (~20°–30°N)

164 Kaolinite, smectite,  $\delta^{18}\text{O}_{\text{carb}}$  and  $\delta^{18}\text{O}_{\text{bel}}$  LOESS smoothing curves are plotted with the  
165 carbon isotope stratigraphy and the biostratigraphic scheme in Fig. 2.

166 The smoothed records of kaolinite and smectite range from 16 to 39 % and from 21 to 43 %,  
167 respectively. The early Valanginian (*Tirnovella pertransiens*–*Busnardoites campylotoxus* ammonite  
168 Zones) is characterized by relatively stable values with averages of 27 and 36 %, despite a small  
169 decreasing/increasing trend in the kaolinite/smectite percentages at the base of the section. Near the  
170 early–late Valanginian transition, i.e. where the Weissert event starts (*B. campylotoxus*–*Saynoceras*  
171 *verrucosum* transition Zones), the kaolinite record shows an increasing trend, reaching a maximum  
172 of 39% at the  $\delta^{13}\text{C}$  climax, whereas the smectite curve displays a drop of 13 % (from 34 to 21 %). A  
173 significant decrease in kaolinite abundances to 16 % is observed throughout the early late  
174 Valanginian (*S. verrucosum*–*Neocomites peregrinus* zones). Smectite reaches contents of up to 41  
175 % in this interval. Finally, the upper part of the section, which covers the late Valanginian interval  
176 (*N. peregrinus*–*Criosarasinella furcillata* zones), shows relatively stable values in kaolinite and  
177 smectite contents, with averages of 22 and 40 %, respectively.

178 The smoothed  $\delta^{18}\text{O}_{\text{carb}}$  record is quite stable in the early Valanginian (Fig. 2), ranging from  
179  $-2.0$  to  $-1.8\text{‰}$ . The oxygen isotope data show a decreasing trend in the early–late Valanginian  
180 transition, and reaches their lowest values ( $-2.4 \text{‰}$ ) at the  $\delta^{13}\text{C}$  peak. The late Valanginian is  
181 characterized by rather scattered  $\delta^{18}\text{O}_{\text{carb}}$  values. However, a long-term positive trend is discernible,  
182 going from  $-2.4$  to  $-1.8 \text{‰}$  (amplitude of  $0.6 \text{‰}$ ). The smoothed  $\delta^{18}\text{O}_{\text{bel}}$  data show relatively stable



183 values (between  $-0.3$  and  $-0.2$  ‰) for the early and early–late Valanginian interval, while a  
184 subsequent increase towards more positive ones (from  $-0.2$  to  $0.3$  ‰) is observed in the remainder  
185 of the late Valanginian.

186

### 187 3.1.2. Proto North Atlantic realm ( $\sim 15$ – $17^\circ\text{N}$ )

188 Kaolinite, smectite,  $\delta^{18}\text{O}_{\text{carb}}$  and  $\text{TEX}_{86}$  LOESS smoothing curves are shown in Fig. 3.

189 Throughout the Valanginian, clay mineral assemblages are largely dominated by smectite  
190 (between 70 and 87 %) with minor contents of kaolinite (between 1 and 8 %) and palygorskite  
191 (between 1 and 5 %). The smoothed  $\delta^{18}\text{O}_{\text{carb}}$  record shows rather stable values (between  $-3.7$  and  
192  $-3.5$  ‰) in the early Valanginian. It is characterized by a prominent negative trend, ranging from  
193  $-3.6$  to  $-4.5$  ‰ at the early–late Valanginian transition, followed by a long-term positive trend  
194 (from  $-4.5$  to  $-3.6$  ‰), in the late Valanginian. The smoothed  $\text{TEX}_{86}$  data displays quite stable  
195 values (between 0.91 and 0.93) along the Valanginian interval.

196

### 197 3.1.3. Southern part of the Boreal realm ( $\sim 35$ – $45^\circ\text{N}$ )

198 Kaolinite, smectite,  $\delta^{18}\text{O}_{\text{lent}}$ ,  $\delta^{18}\text{O}_{\text{biv}}$ , and  $\delta^{18}\text{O}_{\text{bel}}$  LOESS smoothing curves are reported in  
199 Fig. 4.

200 The clay mineral assemblages are largely dominated by kaolinite ( $>70$  %) in the early  
201 Valanginian, and by smectite (up to 80 %) in the late Valanginian. Therefore, the early–late  
202 Valanginian transition is characterized by the notable transition from kaolinite to smectite-  
203 dominated sedimentation of clays.

204 The  $\delta^{18}\text{O}_{\text{lent}}$  and  $\delta^{18}\text{O}_{\text{biv}}$  signals show short-term fluctuations (from  $-0.70$  to  $-1.58$  ‰) in the  
205 lower Valanginian. A subsequent increase to  $0.53$  ‰ is documented for the early–late Valanginian  
206 transition, while in the early part of the late Valanginian, the  $\delta^{18}\text{O}_{\text{lent}}$  and  $\delta^{18}\text{O}_{\text{biv}}$  values display  
207 rather stable values (from  $-0.39$  to  $-0.16$  ‰). Further up section, in the latest Valanginian interval,  
208 they rise from  $-0.28$  to  $0.20$  ‰. The smoothed  $\delta^{18}\text{O}_{\text{bel}}$  curve shows a number of short-term

209 variations in the early and early-late Valanginian as well, with values ranging from -0.9 to -0.2 ‰.  
210 It depicts a long-term positive trend from -0.6 to 0.4 ‰ in the remainder of the late Valanginian.

211

### 212 3.2. Southern Tethyan realm (~53°S)

213

214 The evolution of kaolinite, smectite,  $\delta^{18}\text{O}_{\text{carb}}$ , and  $\text{TEX}_{86}$  LOESS smoothing curves are  
215 shown in Fig. 5.

216 The clay mineral fraction is dominated by smectite (>90 %), while kaolinite is absent. The  
217 smoothed  $\delta^{18}\text{O}_{\text{carb}}$  data are marked by a trend towards more positive values in the late Berriasian-  
218 early Valanginian interval (from -2.3 to -1.6 ‰). They show rather stable values (between -1.7 and  
219 -1.6 ‰) during the early-late Valanginian transition, and depict a small decreasing trend (from -1.6  
220 to -1.3 ‰) along the late Valanginian, which is concomitant to a slight decreasing trend (from 0.66  
221 to 0.63) in the smoothed  $\text{TEX}_{86}$  record.

222

## 223 4. Discussion

224

### 225 4.1. Significance of clay mineral and oxygen isotope signals

226

#### 227 4.1.1. Diagenetic overprint

228 Mineralogical signals hold palaeoenvironmental information, which have possibly been  
229 modified by diagenetic processes (e.g., Friedman and O'Neil, 1977; Chamley, 1989; Frank et al.,  
230 1999; Thiry, 2000). Particularly, clay mineral compositions are sensitive to burial diagenesis, which  
231 may be responsible for the progressive illitization and chloritization of smectite in marly interbeds  
232 and limestone beds, respectively (Friedman and O'Neil, 1977; Deconinck and Debrabant, 1985).  
233 Incipient illitization is characterized by the appearance of R1-type illite smectite mixed-layers as  
234 soon as the maximum burial temperature reaches 60-70°C (Šucha et al., 1993; Lanson et al., 2009).

235 In the studied sections, illitization processes have not been identified (Chamley et al., 1983;  
236 Duchamp-Alphonse et al., 2011; Morales et al., 2015; Charbonnier et al., 2016) and smectite is  
237 largely abundant instead. Besides, Rock-Eval analyses performed on selected samples indicate that  
238  $T_{\max}$  values never exceed 435 °C (Burtner and Warner, 1986; Morales et al., 2015; Charbonnier et  
239 al., 2020), thus indicating a low thermal influence, below the oil window. These  $T_{\max}$  values are  
240 consistent with the occurrence of irregular illite-smectite (I-S) R0 minerals with a high proportion  
241 of smectite layers (>50 %), which indicates a weak thermal diagenesis (Dellisanti et al., 2010).  
242 Therefore, it is reasonable to state that the impact of diagenesis on clay mineral signals was rather  
243 limited, and that trends in this proxy reflect palaeoenvironmental conditions.

244 Published  $\delta^{18}\text{O}_{\text{bel}}$  signals used here have already been previously evaluated for their capacity  
245 to depict primary palaeotemperature signals using trace element geochemistry,  
246 cathodoluminescence, and scanning electron microscope observations (Price et al., 2000, 2018; van  
247 de Schootbrugge et al., 2000; Price and Mutterlose, 2004). The authors highlight no significant  
248 diagenetic or compaction overprints, and suggest that the  $\delta^{18}\text{O}_{\text{bel}}$  signal reflects the isotopic  
249 composition of intermediate waters, belemnite being now considered as nektobenthic organisms  
250 living below the thermocline (50 to 250 m) (e.g., Wierzbowski, 2002; Price et al., 2009, 2012;  
251 Alberti et al., 2012; Jenkyns et al., 2012; Mutterlose et al., 2012; Meissner et al., 2015).

252 Extreme care is needed in the evaluation of the history of sediment preservation when using  
253  $\delta^{18}\text{O}_{\text{carb}}$  as a palaeoenvironmental proxy. Primary whole-rock oxygen isotope ratios are sensitive to  
254 differential compaction processes, as well as early meteoric and burial diagenesis. They all may  
255 lead to fluid-rock interaction, neof ormation/recrystallization of the carbonate phases and thus,  
256 isotopic resetting with later fluids. Rhythmic alternations of green/black marls and/or cherty layers  
257 and limestones are typical sediments of (hemi-) pelagic basins and are specifically present as typical  
258 facies throughout the Early Cretaceous. Some authors show that this bimodal lithologic pattern is  
259 strongly affected by two contrasting diagenetic pathways during the early diagenesis (more  
260 weathering-resistant limestone beds versus softer interbeds) (Reinhardt et al., 2000; Westphal et al.,

261 2000). Model simulations of Ricken (1986, 1987) suggest that the calcium carbonate cement in the  
262 limestone beds was sourced from calcium carbonate dissolution in the interlayers during the early  
263 diagenesis prior to the compaction. They demonstrate that the possible effect of differential  
264 compaction and early diagenetic changes acting on the precursors of these rhythmic marl-limestone  
265 alternations, may have seriously disturbed the original primary signal of  $\delta^{18}\text{O}_{\text{carb}}$  signal (Westphal et  
266 al., 2008). Cyclostratigraphic investigations reveal that marl-limestone alternations in the  
267 Valanginian sediments mainly originate from cyclic changes of humidity/aridity conditions linked  
268 to Earth orbital cycles rather than diagenetic overprint (Cotillon et al., 1980; Sprovieri et al., 2006;  
269 Charbonnier et al., 2013; Martinez et al., 2013, 2015). Diagenetic overprint may also causes  
270 decreases of primary  $\delta^{18}\text{O}_{\text{carb}}$  and  $\delta^{13}\text{C}_{\text{carb}}$  values through the precipitation of variable amounts of  
271 diagenetic cements depleted in  $^{18}\text{O}$  and  $^{13}\text{C}$ , respectively (e.g., Veizer, 1983; Jenkyns and Clayton,  
272 1986; Jenkyns, 1995; Godet et al., 2016; Benamara et al., 2020). Cross plots of  $\delta^{18}\text{O}_{\text{carb}}$ - $\delta^{13}\text{C}_{\text{carb}}$  of  
273 the northwestern Tethyan, Proto North Atlantic, and southern Tethyan realms, reveal lack of  
274 correlations ( $R^2=0.02$ ,  $0.03$ , and  $0.17$ , respectively) (Fig. 6). Besides, no negative or positive  
275 covariance exists between the  $\delta^{18}\text{O}$  signal and the  $\text{CaCO}_3$  contents in the ODP 765C (southern  
276 Tethyan realm) ( $R^2=0.03$ , Fig. S1 in supplementary online materials, SOM) as it would be expected  
277 from strong burial overprint (Frank et al., 1999). The  $\delta^{18}\text{O}_{\text{carb}}$  values studied herein, are similar to  
278 those of open marine carbonates (from  $-4.0$  to  $-1.0$  ‰) and fall generally within the range of  $\delta^{18}\text{O}$   
279 values for sediments from the Early Cretaceous period (Van de Schootbrugge et al., 2000; Godet et  
280 al., 2006; Stein et al., 2011). Burial diagenesis overprint has not significantly affected the primary  
281  $\delta^{18}\text{O}_{\text{carb}}$  signal as suggested by the well-preserved clay mineral assemblage in the signal. Although  
282 this reinforces the assumption that the  $\delta^{18}\text{O}_{\text{carb}}$  trends reflect an original signal, we cannot totally  
283 exclude a potential diagenetic overprint on  $\delta^{18}\text{O}_{\text{carb}}$  absolute values, and thus on reconstructed  
284 palaeotemperatures. Consequently, we only consider the trends of the long-term LOESS-smoothing  
285  $\delta^{18}\text{O}_{\text{carb}}$  curves. In the same way as for published  $\delta^{18}\text{O}_{\text{bel}}$  signals, and because the whole-rock  
286 carbonate fraction is mainly composed of planktic calcareous fossils, we interpret such trends as

287 average surface temperature changes (Godet et al., 2006; Duchamp-Alphonse et al., 2007; Bodin et  
288 al., 2009; Stein et al., 2011).

289 Stable isotope analyses of foraminifera have been used to reconstruct temperatures at  
290 various depths of the water column, depending on the habitat of the studied taxa. Because the shell  
291 of *Lenticulina* spp. is prone to be filled with sediments, the  $\delta^{18}\text{O}_{lent}$  can be contaminated either, by  
292 the sediments itself either, by calcite dissolution processes associated with shell fragmentations.  
293 Selected specimens of *Lenticulina* genera have previously been examined by scanning electron  
294 microscopy (SEM) to assess the degree of diagenetic overprint (Morales et al., 2015). The authors  
295 concluded that foraminifera are composed of primary calcite crystals, since SEM images of shell  
296 structures show tests, pores, and chambers, free of secondary calcite, mural pores depicting well-  
297 defined edges (Morales et al., 2015). *Lenticulina* is a cosmopolitan genus, with low ecological  
298 requirements, that occupied a wide range of microhabitats (from epifaunal to deep infaunal habitats)  
299 (Reolid et al., 2013). The  $\delta^{18}\text{O}_{lent}$  signal might therefore reflect a vertical temperature gradient  
300 between these microhabitats and absolute values in  $\delta^{18}\text{O}_{lent}$  should be considered with extreme  
301 caution. Consequently, we use the isotope trends as a benthic signal, in the only case that they are in  
302 well agreement with  $\delta^{18}\text{O}_{carb}$ , and  $\delta^{18}\text{O}_{bel}$  ones.

303

#### 304 4.1.2. Kaolinite and smectite as palaeoclimate proxies

305 Kaolinite and smectite represent the major clay components in the studied sections.  
306 Palygorskite is observed only at the DSDP Sites retrieved in the Proto North Atlantic realm.

307 The distribution of kaolinite versus smectite is partly controlled by their differential settling  
308 behaviour, which is related to physical segregation during their transport as a function of  
309 differences in size and flocculation capacity (Thiry, 2000; Adatte et al., 2002; Godet et al., 2008).  
310 Indeed, kaolinite is a dense and coarse mineral that settles preferentially closer to the coast, in  
311 shallow-water environments. Conversely, smectite is a fine-grained mineral that tends to settle  
312 much more slowly, in deeper waters and more offshore settings. Consequently, differential settling

313 of kaolinite versus smectite may explain the distribution of clay mineral assemblages along a  
314 platform/basin transect (Thiry, 2000). The sections selected here present lithologies reflecting  
315 hemipelagic, pelagic, or abyssal settings (Table 1).

316 Sedimentary records in the Proto North Atlantic (~15–17°N) realm, situated in pelagic  
317 environments, are characterized by high smectite contents (>80%) and the absence of kaolinite. In  
318 strong contrast, kaolinite constitutes one of the main phases of the clay mineral assemblages in the  
319 hemipelagic successions from the northwestern Tethyan (~20°–30°N) and southern part of the  
320 Boreal (~35–45°N) realms. Based on these observations, differential settling of clay particles may  
321 be postulated as a cause for relatively high smectite (kaolinite) abundances in pelagic (hemipelagic)  
322 environments. However, as for several clay minerals that are known to have localized distributions,  
323 the relative abundances of smectite and kaolinite follow a climate related latitudinal pattern (Ito and  
324 Wagai, 2017). Smectite is predominantly formed under dry and seasonally contrasted conditions, in  
325 mid- and high latitudes. Kaolinite used to precipitate under humid conditions, particularly in  
326 subtropical environment. The occurrence of lateritic and bauxite deposits in the northwestern  
327 Tethyan realm supports the development of intense biogeochemical weathering and the presence of  
328 kaolinite. At the opposite, the presence of evaporitic and calcrete deposits in sediments from the  
329 Proto-North Atlantic realm is a further argument for widespread aridity in this region during the  
330 Early Cretaceous (Chumakov et al., 1995; Scotese, 2001; Hay and Floegel, 2012), and for the  
331 climate-related occurrence of both high amount of smectite and palygorskite in the clay mineral  
332 assemblages. Thus, the absence of kaolinite in pelagic deposits may be well explained by climatic  
333 conditions and not necessarily only by differential settling processes. Therefore, the smoothed  
334 smectite and kaolinite contents are proposed to depict the weathering conditions that prevailed for  
335 each basin (Figs 2–4).

336 In addition, the kaolinite/smectite ratio can be also modulated by sea-level changes during  
337 regressive/transgressive (proximal/distal) cycles (sources) (Adate et al., 2002). There are some  
338 significant discrepancies between the recent reconstructions of Cretaceous global sea-level changes.

339 According to Haq (2014), the early Valanginian is represented by low amplitude sea level changes,  
340 while the late Valanginian is characterized by a long-term sea-level rise. In their recent review, Ray  
341 et al. (2019) document a progressive increase in the magnitude of sea-level changes from the late  
342 Berriasian to the early Valanginian (e.g., Sahagian et al., 1996; Gréselle and Pittet, 2010;  
343 Dujoncquoy et al., 2018), followed by a major sea level fall (~100-150 m) the late early  
344 Valanginian (*Campylotoxus ammonite Zone*), and a significant sea-level rise at the early-late  
345 Valanginian transition (Gréselle and Pittet, 2010; Dujoncquoy et al., 2018). According to these  
346 authors, the late Valanginian would be characterized by a sea-level highstand marked by a series of  
347 lower-amplitude fluctuations (between 25 and 50 m). Despite these discrepancies, it appears that the  
348 trends in sea-level changes are poorly correlated to the distributions of kaolinite and smectite  
349 contents reported herein (Fig. S2 in supplementary online materials), and when major mineralogical  
350 redistributions occur, particularly within the northwestern Tethyan realm, they are usually not  
351 consistent with a sea-level influence. The prominent sea-level fall reported in the late-early  
352 Valanginian by Ray et al. (2019) is associated with relatively stable kaolinite and smectite contents  
353 (Fig. S2 SOM), while the major sea-level rise documented at the early-late Valanginian transition  
354 corresponds to a significant long-term increase in kaolinite contents. During the late Valanginian,  
355 the significant sea-level rise documented by Haq (2014) is associated with increasing smectite  
356 contents. In such a case, clay mineral assemblages could be influenced by sea-level changes rather  
357 than climatic conditions. However, palynological investigations in the Vocontian Basin, considered  
358 as a key climatic indicator, attest to a reduction of hydrolysing conditions in this realm, which is  
359 rather consistent with the increased smectite pattern observed during this time interval (Kujau et al.,  
360 2013).

361 Consequently, in analogy to the clay distribution in modern oceans (Ito and Wagai, 2017),  
362 and because local sedimentary and diagenetic overprints have been shown to bear less weight, we  
363 assume that the stratigraphic distribution of clay minerals captures general patterns in weathering  
364 intensity at a basin scale. However, caution is in order due to the differential settling overprint and

365 sea-level fluctuations.

366 Furthermore, it should be noted here that halmyrolytic alteration of volcanic glass or basalt  
367 may result in the neoformation of smectite (Chamley, 1989). Since widespread magmatism  
368 occurred along the northwestern Australian passive margin due to rifting during the Early  
369 Cretaceous, it is not excluded that smectite retrieved from Hole 765C (Fig. 5) has a volcanic origin  
370 (Compton and Locker, 1992). The distribution of smectite at this site should be treated in this  
371 perspective.

372

#### 373 4.1.3. Oxygen isotopes as a potential palaeothermometer

374 Once diagenetic overprint is excluded, the  $\delta^{18}\text{O}$  data obtained on carbonates from whole  
375 rock samples or belemnite rostra can be related to: (i) temperatures in the environmental setting; (ii)  
376  $\delta^{18}\text{O}_w$  of seawaters as a function of ice sheet volume and freshwater input; or (iii) a mixture of both  
377 (e.g., Frakes and Francis, 1988; Henderson et al., 2000; Mutterlose et al., 2010; Price et al., 2012;  
378 Meissner et al., 2015). In Mesozoic series, bulk-rock oxygen isotope signals have been widely used  
379 to document changes in average SST, and this has been especially the case when the  $\delta^{18}\text{O}$  variations  
380 were in line with overall paleoenvironmental reconstructions (Godet et al., 2006; Duchamp-  
381 Alphonse et al., 2007; Bodin et al., 2009; Stein et al., 2011; Charbonnier et al., 2016). We used the  
382 paleo-temperature equation of Anderson and Arthur (1983) after Epstein et al. (1953) and Craig and  
383 Gordon (1965):

384

$$385 \quad T(^{\circ}\text{C}) = 16.0 - 4.14 (\delta^{18}\text{O}_c - \delta^{18}\text{O}_w) + 0.13 (\delta^{18}\text{O}_c - \delta^{18}\text{O}_w)^2$$

386

387 Where  $\delta^{18}\text{O}_c = \delta^{18}\text{O}$  vs. VPDB of calcite and  $\delta^{18}\text{O}_w = \delta^{18}\text{O}$  vs. VSMOW of seawater. Estimating  
388  $\delta^{18}\text{O}_w$  is problematic because it is variable through geological time (Hudson and Anderson, 1989).  
389 We have reported  $\delta^{18}\text{O}_w$  values based on the simulation of latitudinal Cretaceous surface seawater  
390  $\delta^{18}\text{O}_w$  from Zhou et al. (2008) and derived  $\delta^{18}\text{O}_{\text{seawater}}$  trends calculated by Price et al. (2018). We



391 used a  $\delta^{18}\text{O}_w$  ranging from 0 and  $-0.5\text{‰}$  for seawater located at a paleolatitude between  $\sim 38$  and  
392  $45^\circ\text{N}$ ,  $0.5\text{‰}$  for seawater situated in the Proto-North Atlantic realm, and  $-1.5\text{‰}$  for seawater  
393 located between  $\sim 50$  and  $70^\circ\text{S}$  (Zhou et al., 2008). Recently, Price et al. (2018) have demonstrated  
394 that the composition of seawater from the northwestern Tethyan realm fluctuated around  $1.0\text{‰}$   
395 with more positive  $\delta^{18}\text{O}_{\text{seawater}}$  values in the *Neocomiensiformis* and *Furcillata-Loryi* Zones and  
396 more negative values in the *Verrucosum* Zone. Consequently, we estimate the amplitude of SST  
397 change with  $\delta^{18}\text{O}_w$  values ranging from  $0.4$  to  $1.4\text{‰}$  (Price et al., 2018) (Table 2).

398

## 399 4.2. Latitudinal palaeoclimate reconstructions in the northern hemisphere

400

### 401 4.2.1. Early Valanginian

402 During the early Valanginian, both kaolinite and smectite contents as well as  $\delta^{18}\text{O}_{\text{carb}}$   
403 document no significant temporal changes in the studied realms (i.e. northwestern Tethyan, the  
404 Proto North Atlantic, and the southern part of the Boreal) (Fig. 7). It appears that weathering  
405 intensity and seawater temperatures have remained stable during this time interval. These results  
406 confirm previous  $\text{TEX}_{86}$  measurements (Littler et al., 2011), palynological investigations (Kujau et  
407 al., 2013), and recently reported Mg/Ca ratios (Price et al., 2018), which highlight stable  
408 temperature conditions within the Proto-North Atlantic and the northwestern Tethyan realms,  
409 respectively.

410 Interestingly, kaolinite and smectite distributions show significant variations according to  
411 the studied basin (Figs. 2, 3, and 4). In a similar way as for modern oceans, these regional  
412 modifications are tentatively explained by the presence and influence of latitudinal climate belts  
413 with contrasted hydrolysing conditions on continents (Fig. 8). The high abundance of kaolinite in  
414 sediments from the northwestern Tethyan (up to  $27\%$ ) and southern part of the Boreal (up to  $74\%$ )  
415 realms suggests the existence of an extensive humid subtropical climate belt (at least)  $\sim 20$  to  $45^\circ\text{N}$   
416 (Fig. 8). By contrast, in the Proto North Atlantic realm, kaolinite is uncommon and never exceeds  $8$

417 % (Zemmels et al., 1972; Chamley, 1981; Chamley et al., 1983; Debrabant et al., 1984; Huff,  
418 1993). Large smectite proportions (>70 %) associated with the occurrence of palygorskite might  
419 instead indicate, that a semi-arid climate belt prevailed at about 15°N (Fig. 8).

420

#### 421 4.2.2. Early–late Valanginian transition

422 The early–late Valanginian transition is characterized by a rise in kaolinite contents in the  
423 northwestern Tethyan realm (up to  $12\pm 5$  %), which supports the development of wetter conditions,  
424 as previously documented by local clay mineral, palynological and geochemical data (Kuhn et al.,  
425 2005; Duchamp-Alphonse et al., 2011; Kujau et al., 2013; Charbonnier et al., 2016). Further north  
426 (at ~45°N), this time interval is marked by the replacement of kaolinite by smectite (from 1 to 74  
427 %), highlighting an abrupt change from high to low weathering intensities and thus, from humid to  
428 dry and seasonally contrasted conditions (Fig. 7). This is well supported by change in spore and  
429 pollen assemblages showing an evolution toward more arid climate (Kujau et al., 2013). These  
430 spatio-temporal changes in the weathering mode may point to the southward migration of a  
431 monsoon-like subtropical rain belt during the Weissert episode, as previously proposed by  
432 Duchamp-Alphonse et al. (2014), Morales et al. (2015), and Charbonnier et al. (2016), based on  
433 local climate reconstructions. Our reconstruction permits to postulate a southward shift of  
434 minimally 15° in latitude (from 45 to 30°N) (cf., Morales et al., 2015). At the opposite, as  
435 documented by the dominance of smectite (>80 %) and palygorskite (>8 %) in the Proto-North  
436 Atlantic realm, climate conditions have remained stable and the semi-arid climate belt has prevailed  
437 in this part (Figs. 7 and 8).

438 Interestingly, clear long-term decreases in whole rock  $\delta^{18}\text{O}$  values have been observed in the  
439 northwestern Tethyan (amplitude:  $0.53\pm 0.18$  ‰), and the Proto North Atlantic realms (amplitude:  
440  $0.95\pm 0.18$  ‰) (Figs. 2 and 3). Such coherent trends clearly exclude a significant overprint of the  
441 smoothed- $\delta^{18}\text{O}_{\text{carb}}$  curves by changes in the local water balance of  $\delta^{18}\text{O}_{\text{w}}$  and salinity. Shifts from  
442 more arid to more humid climate modes may explain the heavier ocean-surface  $\delta^{18}\text{O}$  values because

443 of increased continental freshwater storage linked to a phase of accelerated hydrological cycling  
444 (more strongly  $^{18}\text{O}$ -depleted precipitation) (Föllmi, 2012; Wagreich et al., 2014; Wendler et al.,  
445 2016). However, clay mineralogical distributions suggest the occurrence of specific climate belts  
446 with contrasted weathering regime, which is not in favour of a global climate transition mode  
447 between more arid to more humid conditions. Moreover, during this time interval, the calculated  
448  $\delta^{18}\text{O}_{\text{seawater}}$  values from sections in France and Spain are quite stable (Price et al., 2018), which  
449 highlight that the decreases in the  $\delta^{18}\text{O}$  whole-rock signal have not been only linked to changes in  
450 precipitation/evaporation rates. Consequently, an overall warming phase, characterized by  
451 increasing seawater temperatures seems to be the most plausible explanation. In strong contrast,  
452 oxygen-isotope analyses performed on the selection of hand-picked monogeneric benthic  
453 foraminifera (*Lenticulina* spp.) and bivalves in the southern Boreal realm exhibit a significant  
454 positive  $\delta^{18}\text{O}$  excursion (Fig. 4). This trend is coeval to the abrupt change in clay mineral  
455 assemblages (from kaolinite to smectite dominance), which indicate a switch from humid to dry and  
456 seasonally contrasted conditions. A decrease in the flux of freshwater during time of decreased  
457 humidity lead to more positive  $\delta^{18}\text{O}$  values in general. Consequently, the enhanced  $\delta^{18}\text{O}$  values  
458 could reflect local variations in salinity due to the decreased influx of freshwater input into the  
459 ocean (Morales et al., 2015) (Fig. 4). Alternatively, one might argue that benthic organisms may  
460 simply reflecting colder bottom waters or a diagenetic signal.

461 Applying the equation of Anderson and Arthur (1983) and using various  $\delta^{18}\text{O}_w$  values  
462 according to the latitude (Zhou et al., 2008; Price et al., 2018 and see chapter 4.1.3), results in  
463 temperature increases of about  $3\pm 0.9^\circ\text{C}$  in the northwestern Tethyan and about  $5\pm 0.9^\circ\text{C}$  in the Proto  
464 North Atlantic (Table 2). As such, warming appears much more moderate in the northwestern  
465 Tethyan compared to the Proto-North Atlantic. This confirms the lower temperature variability  
466 recently obtained by belemnite Mg/Ca ratios in the Subbetic Domain and the Vocontian basin  
467 during the Weissert Episode (Price et al., 2018). However, these temperatures and changes therein  
468 are in contradiction with  $\text{TEX}_{86}$  records from the Proto North Atlantic realm, which report stable

469 temperature conditions during the early-late Valanginian transition period (Littler et al., 2011). The  
470 causes for this difference can be related to a diagenetic alteration of the  $\delta^{18}\text{O}_{\text{carb}}$  values recorded by  
471 the whole rock signal (see chapter 4.1.1). Alternatively this discrepancy may be related to a  
472 seasonal bias (Sluijs et al., 2006). The  $\text{TEX}_{86}$  proxy is based on the chrenarchaeotal membrane lipid  
473 distribution in sedimentary rocks, which is dependent on SST (Schouten et al., 2003). However, the  
474 highest fluxes of chrenarchaeotal lipids coincide with periods of high phytoplanktonic productivity  
475 and are recorded during summer months (Sluijs et al., 2006). Therefore, the cell number in the  
476 water column depends on the season, and the  $\text{TEX}_{86}$  signal may record an average of the high  
477 summer SSTs (Sluijs et al., 2006), prone to changes with relatively small amplitudes. In all cases,  
478 changes in SST conditions observed in the oxygen-isotope records attest to a warming phase in the  
479 northern hemisphere. Together with the weathering patterns documented by clay mineral data, they  
480 highlight temperate to semi-arid conditions in the Proto North Atlantic, and humid and subtropical  
481 conditions related to a monsoon-like system in the northwestern Tethyan (Fig. 8).

482

#### 483 4.2.3. Late Valanginian

484 During the late Valanginian, kaolinite contents remain low within the Proto North Atlantic  
485 and the southern part of the Boreal realms (<5 %), while they significantly decrease (from 39 to 16:  
486  $23\pm 5$  %) in the northwestern Tethyan realm (Fig. 7). This latter realm appears more sensitive to  
487 changes in hydrological cycling and subsequent erosion and runoff processes, which is consistent  
488 with the idea of the presence of a monsoon-like system. In a wider perspective, smectite dominates  
489 clay mineral assemblages, which points to a diminution in the weathering intensity in the northern  
490 hemisphere, related to the reduction of hydrolysis conditions.

491 The composite whole rock  $\delta^{18}\text{O}$  values in the northwestern Tethyan and in the Proto North  
492 Atlantic realms show long-term trends towards heavier values (amplitudes of  $0.58\pm 0.18$  ‰ and  
493  $0.88\pm 0.18$  ‰, respectively) (Figs. 2 and 3). These trends probably indicate declines in  
494 palaeotemperatures of  $\sim 3\pm 0.9$  and  $5\pm 0.9^\circ\text{C}$ , respectively (see chapter 4.1.3 and Fig. 7). The

495 difference between whole-rock and TEX<sub>86</sub> records can be explained by a substantial seasonal bias  
496 as suggested above (see chapter 4.2.2). Oxygen-isotope records obtained on the benthic  
497 foraminifera (*Lenticulina* spp.) and bivalves in the southern part of the Boreal realm exhibit similar  
498 trends than those documented by the  $\delta^{18}\text{O}_{\text{carb}}$  (amplitude:  $0.48\pm 0.18$  ‰). They imply a cooling of  
499  $2^{\circ}\text{C}\pm 0.9^{\circ}\text{C}$  of bottom waters during the latest Valanginian (Fig. 6), which is in the same range of  
500 magnitude as those previously obtained from the oxygen-isotopic composition and Mg/Ca ratio of  
501 belemnites in the northwestern Tethyan realm ( $\sim 2\pm 0.6^{\circ}\text{C}$ , McArthur et al., 2007; Price et al., 2018)  
502 and oxygen-isotopic composition of benthic fish teeth ( $\sim 3^{\circ}\text{C}$ , Pucéat et al., 2003; Barbarin et al.,  
503 2012). These are also consistent with combined  $\delta^{18}\text{O}_{\text{bel}}$  data sets from the Boreal realm, which  
504 document a significant cooling ( $\sim 2$  to  $\sim 4\pm 0.6^{\circ}\text{C}$ ) from 35 to 65° N, during the late Valanginian  
505 (Meissner et al., 2015) (Fig. 7).

506 From a global perspective, it appears that during the late Valanginian, a warm temperate belt  
507 probably developed in the Boreal, at the expense of the subtropical humid belt of the northwestern  
508 Tethys (Fig. 8). Finally, a stable semi-arid climate belt in the Proto-North Atlantic ( $\sim 15$ - $17^{\circ}\text{N}$ )  
509 occurred throughout the Valanginian (Fig. 8). Interestingly, the palaeoclimatic belts that are  
510 proposed herein, and based upon high-resolution mineralogical and geochemical data are consistent  
511 with those proposed by Chumakov et al. (1995) and Scotese (2001) for the Early Cretaceous, which  
512 were based on sedimentological, mineralogical and paleontological evidences. The occurrence of  
513 lateritic and bauxite deposits in the northwestern Tethys highlights a humid subtropical belt at  $\sim 20$ –  
514  $35^{\circ}\text{N}$  of latitudes. A semi-arid belt is defined in the Proto North Atlantic, with the presence of  
515 evaporites and calcretes. Finally, a warm temperate belt is documented in the high latitudes from  
516  $\sim 35$  to  $65^{\circ}\text{N}$  (Fig. 8).

### 517 518 4.3. Palaeoclimatic reconstruction in the southern hemisphere

519  
520 At ODP Site 765C ( $\sim 53^{\circ}\text{S}$ ), the stable amounts of smectite throughout the entire

521 Valanginian may have resulted from the alteration of basalt and volcanic ash derived from the  
522 northwestern Australian passive margin (see chapter 4.1.2). However, the clay mineral assemblages  
523 in the Weddell Sea basin (~60°S) document the presence of alternating wet and arid seasons  
524 (Robert and Maillot, 1990), thus suggesting that installation of a temperate belt in this realm (Fig.  
525 8). Interestingly, the smoothed  $\delta^{18}\text{O}_{\text{carb}}$  data displays no significant variations throughout the early  
526 and early-late Valanginian transition (Fig. 5), documenting rather constant temperature conditions  
527 (Fig. 7). These results are consistent with seawater palaeotemperature estimations obtained from the  
528 Austral Basin (Argentina, ~60°S), based on  $\delta^{18}\text{O}_{\text{bel}}$  signals, and indicating constant temperatures of  
529 ~25°C during the early Valanginian (Gómez-Dacal et al., 2019). During the late Valanginian, the  
530 composite  $\delta^{18}\text{O}_{\text{carb}}$  signal of ODP Site 765C shows trend towards heavier values (amplitudes of  
531  $0.3 \pm 0.18 \text{ ‰}$ ) (Fig. 5), which may indicate a decline in palaeotemperatures of  $\sim 2 \pm 0.9^\circ\text{C}$ . Such  
532 cooling event appears to be in agreement with the slight cooling trend documented by  $\text{TEX}_{86}$  data in  
533 the ODP Site 766 ( $\sim 1^\circ\text{C}$ ; Littler et al., 2011) (Fig. 5) and the occurrence of *cheirolepidiaceae* leaves  
534 and pollen in the Gippsland and Otway Basins (southeastern Australia) (Tosolini et al., 2014),  
535 which testify for cool and moist conditions in the region during that time interval. It is also  
536 confirmed by recent chronostratigraphic investigations of sedimentary sequences from the southern  
537 and western margins of the Eomanga Basin (~70°S), which indicate a late Valanginian age for  
538 glaciogenic facies, and more particularly for the Living Tillite Member (Alley et al., 2019). In all  
539 cases, these results draw the scenario of a global cooling in both hemispheres during the late  
540 Valanginian.

541

542 4.4. Valanginian climate conditions: a complex interplay between regional versus global  
543 mechanisms

544

545 Our compilation of published and unpublished clay mineral and  $\delta^{18}\text{O}_{\text{carb}}$  data allows for a  
546 better appraisal of global climate conditions during the Valanginian. The low- to mid-latitudes of

547 northern hemisphere are characterized by the presence of two main rainfall belts: a humid  
548 subtropical one associated with a monsoon-like system bringing significant precipitations into the  
549 Tethyan realm, as testified by the important proportions of kaolinite in the area from sites between  
550 (at least) ~20 to 45°N; and a sub-arid one, characterized by dry conditions in the Proto North  
551 Atlantic realm, as documented by prominent proportions of smectite and palygorskite at sites ~15–  
552 17°N. Temperate conditions may have prevailed around 45°N and up to ~60°N.

553 Both hemispheres present distinct features, with a lower temperature gradient through the  
554 early Valanginian in the southern hemisphere than in the northern one, as recently proposed by  
555 Gómez-Dacal et al. (2019). The distribution of climate sensitive sediments also demonstrates that a  
556 complex system develops in the northern hemisphere whereas low- to mid-latitudes of the southern  
557 hemisphere may probably be under the broad influence of an arid climate belt (Chumakov et al.,  
558 1995) (Fig. 8). The climatic asymmetry of hemispheres existed throughout the geological history  
559 (Chumakov, 2004). These general climate conditions are probably related to the overall continental  
560 configuration and particularly the distribution of the oceanic gateways, which modulate circulation  
561 pattern and heat transfer at regional and global scales (Poulsen et al., 2001, 2003; Hotinski and  
562 Toggweiler, 2003; Donnadieu et al., 2006; Goddérís et al., 2014). One of the causes of the  
563 discrepancies in climate evolution between both hemispheres is certainly the fact that the northern  
564 hemisphere was mainly continental, with marine environments mainly restricted to several smaller  
565 basins, whereas the southern hemisphere is divided into one larger continent and a very large ocean.  
566 Particularly, during the earliest Cretaceous, new seaways formed between the Tethyan, the Boreal,  
567 and the Proto North Atlantic realms, due to the fragmentation of the Pangaea (Le Pichon and  
568 Huchon, 1984; Dercourt et al. 1986). A new connection allowed for the establishment of the  
569 westward Tethys Circum global Current (TCC) (Pucéat et al., 2005), which derived from tropical  
570 epicontinental seas around ~20–30°S and brought warm and saline waters to the proto-North  
571 Atlantic Ocean. During the Valanginian, the combination of warm saline surface waters and  
572 restricted palaeogeography in the Proto North Atlantic Ocean probably acted as preconditioning

573 factors for the establishment of a stable and semi-arid belt (Barron et al., 1985; Ziegler et al., 1987;  
574 Hay, 2000, 2008). Under such conditions, the climate is also more sensitive to monsoonal dynamics  
575 due to atmospheric pressure gradients (e.g., Hay, 2008). This may have been the case within the  
576 northwestern Tethyan realm, where the arrangement of continents north and south of the wide  
577 Tethys seaway provided the ideal geographic configuration for significant land–sea pressure  
578 contrasts via the different thermal inertia of land and ocean in this area. These conditions may have  
579 helped maintaining seasonally reversing movements of air mass, heat and precipitation (Oglesby  
580 and Park, 1989), as supported by the important kaolinite deposition in Tethyan and Boreal  
581 sediments in contrast to the Proto North Atlantic (Charbonnier et al., 2016) (Figs. 7 and 8).

582 Superimposed on these regional mechanisms, many studies suggested a link with the  
583 intensification of the Paraná-Etendeka (South America-South Africa) volcanic activity (Lini et al.,  
584 1992; Föllmi et al., 1994; Erba et al., 2004). An update of the Valanginian/Hauterivian  
585 astrochronological time scale confirms a potential link between the main phase of Paraná-Etendeka  
586 volcanic activity ( $-134.6\pm 0.6$ ;  $-134.3\pm 0.8$  Ma; Thiede and Vasconcelos, 2010; Janasi et al., 2011)  
587 and the beginning of the Weissert episode ( $-135.22 \pm 1$  Ma) (Martinez et al., 2015). Moreover, a set  
588 of mercury anomalies in Valanginian sediments recovered from localities outside and in European  
589 sections demonstrated that a main phase of magmatism occurred at the onset of the Weissert  
590 episode (Charbonnier et al., 2017, 2020). Our study highlights a coherent fingerprint of the Paraná-  
591 Etendeka emplacement on climate change across the Weissert Episode. Indeed, the global warming  
592 observed during the Weissert episode is the typical consequence of increased emissions of  
593 greenhouse gases from a LIP volcanism. In contradiction to Price et al. (2018), it appears that  
594 elevated  $p\text{CO}_2$  levels during the Weissert episode and associated warming may have actually  
595 accelerated the hydrological cycle and enhanced nutrient input from continents to ocean. Ocean  
596 fertilization associated with excess of  $\text{CO}_2$  in surface waters (i.e., surface-ocean acidification) may  
597 have induced marine carbonate production crisis in both in neritic and pelagic domains (Föllmi et  
598 al., 1994; Weissert et al., 1998; Erba et al., 2004; Weissert and Erba, 2004; Barbarin et al., 2012;



599 Duchamp-Alphonse et al., 2014). On the continent the development of greenhouse conditions  
600 probably led to the implantation of an important vegetation cover from mid to high latitudes, as  
601 highlighted by widespread coal deposits in the sedimentary records (Ziegler et al., 1987; McCabe  
602 and Totman Parish, 1992; Scotese, 2001; Westermann et al., 2010) (Fig. 8). Particularly, dense  
603 conifer forests of Valanginian age were documented in the Australian (~53–85°S) and Canadian  
604 domains (~74–79°N) (Dettmann et al., 1992; McLoughlin and Hill, 1996; McLoughlin et al., 2002;  
605 Galloway et al., 2013, 2015; Tosolini et al., 2014) (Fig. 8). The presence of extensive polar forests  
606 probably induced positive feedbacks between climate and vegetation, reducing surface albedo and  
607 increasing adsorption of solar radiation at high latitudes (Upchurch et al., 1998). During the  
608 Valanginian these factors might have also played an important role in maintaining high-latitude  
609 warmth, which might have induced the presence of a stable warm temperate belt in high latitudes  
610 (Fig. 8). This is supported by clumped-isotope analyses from belemnites, which testify for warm  
611 polar conditions (10–20°C) at 60–65°N (Price and Passey, 2013). The long-lasting and global burial  
612 of terrestrial organic carbon consuming a significant amount of atmospheric CO<sub>2</sub>, may have  
613 contributed to the global cooling observed in both hemispheres, during the last stages of the  
614 Weissert episode (Figs. 7 and 8). In fossil plant material, from the late Valanginian, Gröcke et al.  
615 (2005) attested cool terrestrial conditions caused by a decrease in atmospheric *p*CO<sub>2</sub> levels.  
616 Stratigraphic and sedimentological evidences suggest that this global cold event may have help  
617 developing the Livingston glaciation observed in high southern latitudes during the late  
618 Valanginian–Hauterivian interval (Alley et al., 2019). One cannot exclude that this time interval  
619 might also be punctuated by limited extension of polar ice cap in the high northern latitudes, as  
620 previously documented by the occurrence of glendonites, tillites, and dropstones described in  
621 Svalbard (~65–70°N; Kemper and Schmitz, 1975; Price and Nunn, 2010; Vickers et al., 2019), in  
622 the Sverdrup Basin (~74–79°N; Kemper, 1987; Price, 1999), and in Siberia (Price, 1999). Such cold  
623 conditions could have caused the formation of a new deep-water ocean current system through the  
624 opening of the Greenland-Norwegian seaway (Pauly et al., 2012).

625

## 626 **5. Conclusions**

627

628 The set of published and unpublished mineralogical and geochemical data presented in this  
629 study allows to show the reliability of clay and  $\delta^{18}\text{O}_{\text{carb}}$  data as good palaeoclimate proxies for the  
630 Valanginian.

631 In the northern hemisphere, the kaolinite and smectite distributions obtained through the  
632 Valanginian show significant variations, which can be tentatively explained by the presence of  
633 latitudinal climatic belts characterized by contrasted hydrolysing conditions. It appears that stable  
634 semi-arid conditions prevailed through the Valanginian in the Proto North Atlantic realm (~15–  
635 17°N), and a humid subtropical climatic belt was present between (at least) ~20 and 45°N. Spatio-  
636 temporal changes in the weathering mode (from ~30 to 45°N), from humid to dry and seasonally  
637 contrasted conditions, clearly points to the southward migration of a monsoon-like rain tropical belt  
638 in the northwestern Tethyan realm during the Weissert episode. The general trends in the  $\delta^{18}\text{O}_{\text{carb}}$   
639 records reveal that the northern hemisphere was characterized by an overall warming phase at the  
640 early–late Valanginian transition, with temperatures increasing between ~3 and  $5\pm 0.9^\circ\text{C}$ . Our data  
641 suggest also a significant and generally long-term cooling trend throughout the late Valanginian  
642 between ~1 and  $5\pm 0.9^\circ\text{C}$  in both hemispheres. In strong contrast, it appears that the amplitude of  
643 climatic changes recorded during the Valanginian was probably less pronounced in the southern  
644 hemisphere than in the northern one.

645 Climate evolution during the Valanginian resulted from the complex interplay between  
646 regional, global, palaeogeographic and palaeoceanographic impacts and changes therein, which  
647 influenced the exchange of currents, and especially heat flow, and which triggered the development  
648 of a dense vegetation cover on the continents, capable of preserving excess carbon in the form of  
649 terrestrial organic matter (leading to the formation of widespread coal deposits). However, further  
650 investigations are needed in the southern hemisphere and at a global scale, to better detail the  
651 climate regime of the Valanginian.

652

653 **Acknowledgments**

654

655 We are grateful for the advices and help of Corinne Fesneau for clay mineral analyses in the  
656 northwestern Tethys sections. We appreciated also the help of Tiffany Monnier for laboratory  
657 assistance. We thank the Swiss National Science Foundation (project 200021\_168994) and the  
658 University of Lausanne for financial and logistic supports. We would also like to acknowledge the  
659 help of editor Alessandra Negri and the constructive comments of two anonymous reviewers.

660

661 **References**

662

663 Adatte, T., Keller, G., Stinnesbeck, W., 2002. Late Cretaceous to Early Palaeocene climate and sea-  
664 level fluctuations: the Tunisian record. *Palaeogeography, Palaeoclimatology, Palaeoecology*  
665 178, 165–196.

666 Aguado, R., Company, M., Castro, J.M., de Gea, G.A., Molina, J.M., Nieto, L.M., Ruiz-Ortiz, P.A.,  
667 2018. A new record of the Weissert episode from the Valanginian succession of Cehegín  
668 (Subbetic, SE Spain): bio- and carbon isotope stratigraphy. *Cretaceous Research* 92 122–137.

669 Alberti, M., Fürsich, F.T., Pandey, D.K., 2012. The oxfordian stable isotope record ( $\delta^{18}\text{O}$ ,  $\delta^{13}\text{C}$ ) of  
670 belemnites, brachiopods, and oysters from the Kachchh Basin (western India) and its potential  
671 for palaeoecologic, palaeoclimatic, and palaeogeographic reconstructions. *Palaeogeography,*  
672 *Palaeoclimatology, Palaeoecology* 344-345, 49–68.

673 Alley, N.F., Frakes, L.A., 2003. First know Cretaceous glaciation: Livingston tillite member of the  
674 Cadna-owie Formation, South Australia. *Australian Journal of Earth Sciences* 50, 139–144.

675 Alley, N.F., Hore, S.B., Frakes, L.A., 2019. Glaciations at high-latitude Southern Australia during  
676 the Early Cretaceous. *Australian Journal of Earth Science* DOI:  
677 10.1080/08120099.2019.1590457.

- 678 Anderson, T.F., Arthur, M.A., 1983. Stable isotopes of oxygen and carbon and their application to  
679 sedimentologic and paleoenvironmental problems. In: Arthur, M.A., Anderson, T.F., Kaplan,  
680 I.R., Veizer, J., Land, L.S. (Eds.), *Stable Isotopes in Sedimentary Geology*. SEPM Short  
681 Course, Tulsa. 1–151.
- 682 Bajnai, D., Pálffy, J., Martinez, M., Price, G.D., Nyerges, A., Főzy, I., 2017. Multi-proxy record of  
683 orbital-scale changes in climate and sedimentation during the Weissert event in the  
684 Valanginian Bersek Marl Formation (Gerecse Mts., Hungary). *Cretaceous Research* 75, 45-  
685 60.
- 686 Barbarin, N., Bonin, A., Mattioli, E., Pucéat, E., Cappetta, H., Gréselle, B., Pittet, B., Vennin, E.,  
687 Joachimski, M., 2012. Evidence for a complex Valanginian nannoconid decline in the  
688 Vocontian basin (South East France). *Marine Micropaleontology* 84–85, 37–53.
- 689 Barron, E. J., Arthur, M.A., Kauffman E.G., 1985. Cretaceous rhythmic bedding sequences: A  
690 plausible link between orbital variations and climate, *Earth and Planetary Science Letters* 72,  
691 327–340.
- 692 Blakey, R., 2010. Early Cretaceous European paleogeographic map. Available online  
693 [http://cpgeosystems.com/125\\_Cret\\_EurMap\\_sm.jpg](http://cpgeosystems.com/125_Cret_EurMap_sm.jpg) (21.10.2010).
- 694 Benamara, A., Charbonnier, G., Adatte, T., Spangenberg, J.E., Föllmi, K.B., 2020. Precession-  
695 driven monsoonal activity controlled the development of the early Albian Paquier oceanic  
696 anoxic event (OAE1b): Evidence from the Vocontian Basin, SE France. *Palaeogeography,*  
697 *Palaeoclimatology, Palaeoecology* 537, 109406.
- 698 Bennett, M.R., Doyle, P., Mather, A.E. and Woodfin, J., 1994. Testing the climatic significance of  
699 dropstones: an example from the Miocene of the Sorbas Basin, south east Spain. *Geol. Mag.*,  
700 131: 845-848.
- 701 Bennett, M.R., Doyle, P., Mather, A.E., 1996. Dropstones: their origin and significance.  
702 *Palaeogeogr. palaeoclimatol. palaeoecol.* 121, 331 – 339.
- 703 Bodin, S., Fiet, N., Godet, A., Matera, V., Westermann, S., Clément, A., Janssen, N.M.M., Stille,

704 P., Föllmi, K.B., 2009. Early Cretaceous (late Berriasian to early Aptian) palaeoceanographic  
705 change along the northwestern Tethyan margin (Vocontian Trough, southeastern France):  
706  $\delta^{13}\text{C}$ ,  $\delta^{18}\text{O}$  and Sr-isotope belemnite and whole-rock records. *Cretaceous Research* 30, 1247-  
707 1262.

708 Bornemann, A., Mutterlose, J., 2008. Calcareous nannofossil and  $\delta^{13}\text{C}$  records from the Early  
709 Cretaceous of the western Atlantic ocean: evidence for enhanced fertilization across the  
710 Berriasian–Valanginian transition. *Palaios* 23, 821–832.

711 Burtner R.L., Warner M.A., 1986. Relationship between illite/smectite diagenesis and hydrocarbon  
712 generation in Lower Cretaceous Mowry and Skull Creek Shales of the Northern Rocky  
713 Mountain area. *Clays and Clay Minerals*, 34, 390-402.

714 Chamley, H., 1981. Long-term trends in clay deposition in the ocean. *Oceanol. Acta*, 3P: 105-110.

715 Chamley, H., 1989. *Clay Sedimentology*. Springer-Verlag, Berlin. 623 pp.

716 Chamley, H., Debrabant, P., Candillier, A.-M., Foulon, J., 1983. Clay mineralogical and inorganic  
717 geochemical stratigraphy of Blake-Bahama Basin since the Callovian, site 534, Deep Sea  
718 Drilling Project, Leg 76. In Sheridan, R. E., Gradstein, F. M., et al., *Init. Repts. DSDP*, 76:  
719 Washington (U.S. Govt. Printing Office), 437-448.

720 Channell, J.E.T., Erba, E., Lini, A., 1993. Magnetostratigraphic calibration of the late Valanginian  
721 carbon isotope event in pelagic limestones from northern Italy and Switzerland. *Earth and  
722 Planetary Science Letters* 118, 145–166.

723 Charbonnier, G., Boulila, S., Gardin, S., Duchamp-Alphonse, S., Adatte, T., Spangenberg, J.E.,  
724 Föllmi, K.B., Colin, C., Galbrun, B., 2013. Astronomical calibration of the Valanginian  
725 “Weissert” episode: the Orpierre marl-limestone succession (Vocontian Basin, southeastern  
726 France). *Cretaceous Research* 45, 25–42.

727 Charbonnier, G., Duchamp-Alphonse, S., Adatte, T., Föllmi, K.B., Spangenberg, J.E., Gardin, S.,  
728 Galbrun, B., Colin, C., 2016. Eccentricity paced monsoon-like system during the Valanginian  
729 (Early Cretaceous) new insights from detrital and nutrient fluxes into the Vocontian Basin

730 (SE France): Palaeogeography, Palaeoclimatology, Palaeoecology 443, 45-155.

731 Charbonnier, G., Morales, C., Duchamp-Alphonse, S., Westermann, S., Adatte, T., and Föllmi,  
732 K.B., 2017. Mercury enrichments indicate volcanic triggering of Valanginian environmental  
733 change: Scientific Reports DOI:10.1038/srep40808.

734 Charbonnier, G., Adatte, T., Duchamp-Alphonse, S., Spangenberg, J.E., Föllmi K.B., 2020. Global  
735 mercury enrichment in Valanginian sediments supports a volcanic trigger for the Weissert  
736 episode, in Adatte, T., Bond, D.P.G., and Keller, G., eds., Mass Extinctions, Volcanism, and  
737 Impacts: New Developments: Geological Society of America Special Paper 544, p.

738 Chumakov, N.M., 2004. Trends in global climate changes inferred from geological data.  
739 Stratigraphy and Geological Correlation 12, 117-138.

740 Chumakov, N.M., Zharkov, M.A., Herman, A.B., Doludenko, M.P., Kalandadze, N.N., Lebedev,  
741 E.A., Ponomarenko, A.G., Rautian, A.S., 1995. Climate belts of the Mid- Cretaceous time.  
742 Stratigraphy and Geological Correlation 3, 241–260.

743 Cleveland, W.S., Devlin, S.J., 1988. Locally weighted regression: an approach to regression  
744 analysis by local fitting. Journal of America State Association 83, 596–610.

745 Cotillon, P., Rio, M., 1984. Cyclic sedimentation in the Cretaceous of DSDP site 535 and 540 (Gulf  
746 of Mexico), 534 (central Atlantic) and the Vocontian Basin (France). In: Buffler, R.T.,  
747 Schlager, W., Pisiotto, K.A. (Eds), Initial Reports of the Deep Sea Drilling Project 77, 339–  
748 376.

749 Cotillon, P., Ferry, S., Gaillard, C., Jautée, E., Latreille, G., Rio, M., 1980. Fluctuations des  
750 paramètres du milieu marin dans le domaine Vocontien (France du Sud-Est) au Crétacé  
751 inférieur: mise en évidence par l'étude de formations marno- calcaires alternantes. Bulletin de  
752 la Société Géologique de France 22, 735–744.

753 Compton, J.S., Locker, S.D., 1992. Diagenesis of clay and silicaminerals in sediments from the  
754 Argon Basin, Northeastern Indian Ocean (Site 765). Proc. ODP program,  
755 Scientific Results, 123, 57-75.

756 Craig, H., Gordon, L.I., 1965. Deuterium and oxygen-18 variations in the ocean and the marine  
757 atmosphere. Proceedings of a Conference on Stable Isotopes in Oceanographic Studies and  
758 Paleotemperatures, Spoleto, Italy, pp. 9–130.

759 Debrabant, P., Chamley, H., Foulon, J., 1984. Paleoenvironmental implications of mineralogic and  
760 geochemical data in the western Florida Straits (leg 77, deep sea drilling project). Initial  
761 Reports. DSDP, 11: Washington (U.S. Gouvernement. Printing Office).

762 Deconinck, J.-F., Debrabant, P., 1985. Diagenèse des argiles dans le domaine subalpin: rôles  
763 respectifs de la lithologie, de l'enfouissement et de la surcharge tectonique. *Revue de*  
764 *Géologie Dynamique et de Géographie Physique* 26, 321–330.

765 Dellisanti, F., Pini, G.A., Baudin, F., 2010. Use of  $T_{max}$  as a thermal maturity indicator in orogenic  
766 successions and comparison with clay mineral evolution. *Clay Minerals* 45(1), 115-130.

767 Dercourt, J., Zonenshain, L.P., Ricou, L.E., Kazmin, V.G., Le Pichon, X., Knipper, A.L.,  
768 Grandjacquet, C., Sborshchikov, I.M., Boulin, J., Sorokhtin, O., Geysant, J., Lepvrier, C.,  
769 Biju-Duval, B., Sibuet, J.C., Sayostin, L.A., Westphal, M., Lauer, J.P., 1986. Geological  
770 evolution of the Tethys belt from the Atlantic to the Pamir since the Lias. *Tectonophysics*  
771 123, 241–315.

772 Dettmann, M.E., Molnar, R.E., Douglas, J.G., Burger, D., Fielding, C., Clifford, H.T., Francis, J.,  
773 Jell, P., Rich, T., Wade, M., Rich, P.V., Pledge, N., Kemp, A., Rozefelds, A., 1992.  
774 Australian Cretaceous terrestrial faunas and floras: biostratigraphic and biogeographic  
775 implications. *Cretaceous Research* 13, 207–262.

776 Ditchfield, P.W., 1997. High northern palaeolatitude Jurassic–Cretaceous palaeotemperature  
777 variation: New data from Kong Karls Land, Svalbard. *Palaeogeogr. Palaeoclimatol.*  
778 *Palaeoecol.* 130, 163–175.

779 Donnadieu, Y., Pierrehumbert, R., Jacob, R., Fluteau, F., 2006. Modelling the primary control of  
780 paleogeography on Cretaceous climate. *Earth and Planetary Science Letters* 248, 426–437.

781 Doublet, S., Garcia, J.P., 2004. The significance of dropstones in a tropical lacustrine setting,

782 eastern Cameros Basin (Late Jurassic-Early Cretaceous, Spain). *Sedimentary Geology* 163,  
783 293-309.

784 Duchamp-Alphonse, S., Fiet, N., Adatte, T., Pagel, M., 2011. Climate and sea-level variations along  
785 the northwestern Tethyan margin during the Valanginian C-isotope excursion: mineralogical  
786 evidence from the Vocontian Basin (SE France). *Palaeogeography, Palaeoclimatology,*  
787 *Palaeoecology* 302, 243–254.

788 Duchamp-Alphonse, S., Gardin, S., Fiet, N., Bartolini, A.C., Blamart, D., Pagel, M., 2007.  
789 Fertilization of the northwestern Tethys (Vocontian basin, SE France) during the Valanginian  
790 carbon isotope perturbation: evidence from calcareous nannofossils and trace element data.  
791 *Palaeogeography, Palaeoclimatology, Palaeoecology* 243, 132–151.

792 Duchamp-Alphonse, S., Gardin, S., Bartolini, A., 2014. Calcareous nannofossil response to the  
793 Weissert episode (Early Cretaceous): Implications for palaeoecological and  
794 palaeoceanographic reconstructions. *Marine Micropaleontology* 113, 65-78.

795 Dujoncquois, E., Grélaud, C., Razin, P., Imbert, P., van Buchem, F., Dupont, G., Le Bec, A., 2018.  
796 Seismic stratigraphy of a lower Cretaceous prograding carbonate platform (Oman) and  
797 implications for the eustatic sea-level curve. *AAPG Bulletin* 102, 509–543.

798 Epstein, S., Buchsbaum, R., Lowenstam, H.A., Urey, H.C., 1953. Revised carbonate-water isotopic  
799 temperature scale. *Geol. Soc. Am. Bull.* 64, 1315–1326.

800 Erba, E., Tremolada, F., 2004. Nannofossil carbonate fluxes during the early Cretaceous:  
801 phytoplankton response to nutrification episodes, atmospheric CO<sub>2</sub>, and anoxia.  
802 *Paleoceanography* 19, 1–18.

803 Erba, E., Bartolini, A.C., Larson, R.L., 2004. Valanginian Weissert oceanic anoxic event. *Geology*  
804 32, 149–152.

805 Föllmi, K.B., 2012, Early Cretaceous life, climate and anoxia. *Cretaceous Research*, v. 35, p. 230-  
806 257.

807 Föllmi, K.B., Weissert, H., Bisping, M., Funk, H., 1994. Phosphogenesis, carbon-isotope



808 stratigraphy, and carbonate-platform evolution along the Lower Cretaceous northern Tethyan  
809 margin. *Geological Society of American Bulletin* 106, 729–746.

810 Föllmi, K.B., Godet, A., Bodin, S., Linder, P., 2006. Interactions between environmental change  
811 and shallow water carbonate build-up along the northern Tethyan margin and their impact on  
812 the early Cretaceous carbon isotope record. *Paleoceanography*, 21, 1–16.

813 Fozy, I., Janssen, N.M.M., Price, G.D., Knauer, J., Palfy, J., 2010. Integrated isotope and  
814 biostratigraphy of a Lower Cretaceous section from the Bakony Mountains (Transdanubian  
815 Range, Hungary): a new Tethyan record of the Weissert event. *Cretaceous Research* 31, 525–  
816 545.

817 Frakes, L.A., Francis, J.E., 1988. A guide to Phanerozoic cold polar climates from highlatitude ice-  
818 rafting in the Cretaceous. *Nature* 333, 547–549.

819 Frakes, L.A., Francis, J.E., Syktus, J.I., 1992. *Climate Modes of the Phanerozoic*. Cambridge Univ.  
820 Press, Cambridge, 274 pp.

821 Frank, T.D, Arthur, M.A., Dean W.E., 1999. Diagenesis of lower Cretaceous pelagic carbonates,  
822 North Atlantic: Paleoceanographic signals obscured, *Journal of Foraminiferal research*, 29, 4,  
823 340–351.

824 Friedman, I., O’Neil, J.R., 1977. *Compilation of stable isotope fractionation factors of geochemical*  
825 *interest*. U.S.G.S. Professional Paper 440-KK.

826 Galloway, J.M., Sweet, A.R., Swindles, G.T., Dewing, K., Haldari, T., Embry, A.F., Sanei, H.,  
827 2013. Middle Jurassic to Lower Cretaceous paleoclimate of Sverdrup Basin, Canadian Arctic  
828 Archipelago inferred from the palynostratigraphy. *Marine and Petroleum Geology* 44, 240–  
829 255.

830 Galloway, J.M., Tullius, D.N., Evenchick, C.A., Swindles, G.T., Hadlari, T., Embry, A., 2015.  
831 Early Cretaceous vegetation and climate change at high latitude: Palynological evidence from  
832 Isachsen Formation, Arctic Canada. *Cretaceous Research* 56, 399-420.

833 Godd ris, Y., Donnadi u, Y., Le Hir, G., Lefebvre, V., Nardin, E., 2014. *Earth-Science Reviews*

834 128, 122-138.

835 Godet, A., Bodin, S., Föllmi, K.B., Vermeulen, J., Gardin, S., Fiet, N., Adatte, T., Berner, Z.,  
836 Stüben, D., van de Schootbrugge, B., 2006. Evolution of the marine stable carbon isotope  
837 record during the Early Cretaceous: A focus on the late Hauterivian and Barremian in the  
838 Tethyan realm. *Earth and Planetary Science Letters* 242, 254–271.

839 Godet, A., Bodin, S., Adatte, T., and Föllmi, K.B., 2008, Platform-induced clay-mineral  
840 fractionation along a northern Tethyan basin-platform transect: implications for the  
841 interpretation of Early Cretaceous climate change (late Hauterivian-early Aptian): *Cretaceous*  
842 *Research* v. 29, p. 830–847.

843 Godet, A., Durllet, C., Spangenberg, J.E., Föllmi, K.B., 2016. Estimating the impact of early  
844 diagenesis on isotope records in shallow-marine carbonates: A case study from the Urgonian  
845 Platform in western Swiss Jura. *Paleogeography, Paleoclimatology, Paleoecology* 454, 125–  
846 138.

847 Gómez-Dacal, A.R., Richiano, S.M., Gómez-Peral, L.E., Spalletti, L.A., Sial, A.N., Poiré, D.G.,  
848 2019. Evidence of warm seas in high latitudes of southern South America during the Early  
849 Cretaceous. *Cretaceous Research* 95, 8-20.

850 Graziano, R., 1999. The early Cretaceous drowning unconformities of the Apulia carbonate  
851 platform (Gargano Promontory, southern Italy): local fingerprints of global  
852 palaeoceanographic events. *Terra Nova* 11, 245–250.

853 Gréselle, B., Pittet, B., 2010. Sea-level reconstructions from the Peri-Vocontian Zone (South-east  
854 France) point to Valanginian glacio-eustasy. *Sedimentology* 57, 1640–1684.

855 Gréselle, B., Pittet, B., Mattioli, E., Joachimski, M., Barbarin, N., Riquier, L., Reboulet, S., Pucéat,  
856 E., 2011. The Valanginian isotope event: a complex suite of palaeoenvironmental  
857 perturbations. *Palaeogeography, Palaeoclimatology, Palaeoecology* 306, 41–57.

858 Gröcke, D.R., Price, G.D., Robinson, S.A., Baraboshkin, E.Y., Mutterlose, J., Ruffell, A.H., 2005.  
859 The Upper Valanginian (Early Cretaceous) positive carbon-isotope event recorded in

860 terrestrial plants. *Earth and Planetary Science Letters* 240, 495–509.

861 Hallam, A., 1985. A review of Mesozoic climates. *Journal of the Geological Society of London*  
862 142, 433–445.

863 Haq, B.U., 2014. Cretaceous eustasy revisited. *Glob. Planet. Chang.* 113, 44–58

864 Hay, W.W., 2000. Climate models for a warm Earth – is something missing? *EOS, Transactions*  
865 *American Geophysical Union* 81 (48 Suppl), F695.

866 Hay, W.W., 2008. Evolving ideas about the Cretaceous climate and ocean circulation, *Cretaceous*  
867 *Research*, 29, 725–753.

868 Hay, W.W., Floegel, S., 2012. New thoughts about the Cretaceous climate and oceans. *Earth-*  
869 *Science Reviews* 115, 262–272.

870 Henderson, R.A., Crampton, J.S., Dettmann, M.E., Douglas, J.G., Haig, D., Shafik, S., Stilwell,  
871 J.D., Thulborn, R.A., 2000. Biogeographical observations on the Cretaceous biota of  
872 Australasia. *Memoirs of the Association of Australian Palaeontologists* 23, 355–404.

873 Hotinski, R.M., Toggweiler, J.R., 2003. Impact of a Tethyan circumglobal passage on ocean heat  
874 transport and “equable” climate. *Paleoceanography* 18, doi: 10.1029/2001PA000730.

875 Hudson, J.D., Anderson, T.F., 1989. Ocean temperatures and isotopic compositions through time.  
876 *Transactions of the Royal Society of Edinburgh* 80, 183–192.

877 Huff, W.D., 1993. Cretaceous clay mineralogy of the continental rise off the east coast of the united  
878 states, site 603, deep sea drilling project leg 93. Initial reports DSDP Washington (US.  
879 Government Printing office.

880 Ito, A., Wagai, R., 2017. Global distribution of clay-size minerals on land surface for  
881 biogeochemical and climatological studies *Scientific Data* 4:170103/DOI: 10.1038/sdata.  
882 2017.103.

883 Janasi, V.D., de Freitas, V.A., and Heaman, L.H., 2011, The onset of flood basalt volcanism,  
884 Northern Parana Basin, Brazil: a precise U–Pb baddeleyite/zircon age for a Chapeco-type  
885 dacite: *Earth and Planetary Science Letters*, v. 302, p. 147–153.

- 886 Jenkyns, H.C., 1995. Carbon-isotope stratigraphy and paleoceanography: Significance of the Lower  
887 Cretaceous shallow water carbonates of Resolution Guyot, Mid Pacific Mountains,  
888 Proceedings of Oceanic Drilling Progress Scientific Report, 143, 99–104.
- 889 Jenkyns, H.C., 2010. Geochemistry of oceanic anoxic events. *Geochemistry, Geophysics,*  
890 *Geosystems* v. 11, p. 1-30.
- 891 Jenkyns, H.C., Clayton, C.J., 1986. Black shales and carbon isotopes in pelagic sediments from the  
892 Tethyan Lower Jurassic. *Sedimentology* 33, 87-106.
- 893 Jenkyns, H.C., Schouten-Huibers, L., Schouten, S., Sinninghe Damsté, J.S., 2012. Warm Middle  
894 Jurassic-Early Cretaceous high-latitude sea-surface temperatures from the Southern Ocean.  
895 *Climate of the Past* 8, 215–226.
- 896 Kemper, E., 1987. Das Klima der Kreide-Zeit. *Geol. Jahrb., Reihe A* 96, 5–185.
- 897 Kemper, E., Schmitz, H.-H., 1975. Stellate nodules from the upper Deer Bay Formation  
898 (Valanginian) of Arctic Canada. *Geological Survey of Canada Paper* 75, 109–119.
- 899 Kuhn, O., Weissert, H., Föllmi, K.B., Hennig, S., 2005. Altered carbon cycling and trace-metal  
900 enrichment during the late Valanginian and early Hauterivian. *Eclogae Geologicae Helvetiae*  
901 98, 333–344.
- 902 Kujau, A., Heimhofer, U., Ostertag-Henning, C., Gréselle, B., Mutterlose, J., 2012. No evidence for  
903 anoxia during the Valanginian carbon isotope event-An organic-geochemical study from the  
904 Vocontian Basin, SE France. *Global and Planetary Change* 92-93, 92–104.
- 905 Kujau, A., Heimhofer, U., Hochuli, P.A., Pauly, S., Morales, C., Adatte, T., Föllmi, K., Ploch, I.,  
906 Mutterlose, J., 2013. Reconstructing Valanginian (early Cretaceous) mid-latitude vegetation  
907 and climate dynamics based on spore-pollen assemblages. *Review of Palaeobotany and*  
908 *Palynology* 197, 50–69.
- 909 Lanson, B., Sakharov, B.A., Claret, F., Drits, V.A., 2009. Diagenetic smectite-to-illite transition in  
910 clay-rich sediments: A reappraisal of X-ray diffraction results using the multi-specimen  
911 method. *American Journal of Science* 309(6), 476-516.

912 Le Pichon, X., P. Huchon 1984. Geoid, Pangea and convection, *Earth Planetary Science Letters* 67,  
913 123–135.

914 Lini, A., Weissert, H., Erba, E., 1992. The Valanginian carbon isotope event: a first episode of  
915 greenhouse climate conditions during the Cretaceous. *Global Change Special Issue: Terra Nova*  
916 4, 374–384.

917 Littler, K., Robinson, S.A., Bown, P.R., Nederbragt, A.J., Pancost, R.D., 2011. High sea-surface  
918 temperatures during the Early Cretaceous Epoch. *Nature Geoscience* 4, 169–172.

919 Martinez, M., Deconinck, J.F., Pellenard, P., Reboulet, S., Riquier, L., 2013. Astrochronology of  
920 the Valanginian stage from reference sections (Vocontian Basin, France) and  
921 palaeoenvironmental implications for the Weissert Event. *Palaeogeography,*  
922 *Palaeoclimatology, Palaeoecology* 376, 91–102.

923 Martinez, M., Deconinck, J.F., Pellenard, P., Riquier, L., Company, M., Reboulet, S., Moiroud, M.,  
924 2015. Astrochronology of the Valanginian-Hauterivian stages (Early Cretaceous):  
925 chronological relationships between the Paraná-Etendeka large igneous province and the  
926 Weissert and the Faraoni events. *Global and Planetary Change* 131, 158–173.

927 McArthur, J.M., Janssen, N.M.M., Reboulet, S., Leng, M.J., Thirlwall, M.F., van de Schootbrugge,  
928 B., 2007. Palaeotemperatures, polar ice-volume, and isotope stratigraphy (Mg/Ca,  $\delta^{18}\text{O}$ ,  $\delta^{13}\text{C}$ ,  
929  $^{87}\text{Sr}/^{86}\text{Sr}$ ): The Early Cretaceous (Berriasian, Valanginian, Hauterivian). *Palaeogeography,*  
930 *Palaeoclimatology, Palaeoecology* 248, 391–430.

931 McArthur, J.M., Mutterlose, J., Price, G.D., Rawson, P.F., Ruffell, A., Thirlwall, M.F., 2004.  
932 Belemnites of Valanginian, Hauterivian and Barremian age: Sr-isotope stratigraphy,  
933 composition ( $^{87}\text{Sr}/^{86}\text{Sr}$ ,  $\delta^{13}\text{C}$ ,  $\delta^{18}\text{O}$ , Na, Sr, Mg), and palaeoceanography. *Palaeogeography,*  
934 *Palaeoclimatology, Palaeoecology* 202, 253–272.

935 McCabe, P.J., Totman Parrish, J., 1992. Tectonic and climatic controls on the distribution and  
936 quality of Cretaceous coals. In: McCabe, P.J., Totman Parrish, J. (Eds.), *Controls on the*  
937 *Distribution and Quality of Cretaceous Coals: Geological Society of America, Special*

938 Publication, vol. 267, pp. 1–16.

939 McLoughlin, S., Hill, R.S., 1996. The succession of Western Australian Phanerozoic floras. In:  
940 Gondwanan Heritage: past, present and future of the Western Australian biota. In: Hopper,  
941 S.D., Chappill, J.A., Harvey, M.S., George, A.S. (Eds.), Proceedings of the Conference on  
942 Systematics, Evolution and Conservation of the Western Australian Biota, Perth, 1993. Surrey  
943 Beatty, Sydney, pp. 61–80.

944 McLoughlin, S., Tosolini, A.M.P., Nagalingum, N.S., Drinnan, A.N., 2002. Early Cretaceous  
945 (Neocomian) flora and fauna of the Lower Strzelecki Group, Gippsland Basin, Victoria.  
946 Memoir 26 of the Association of Australasian Paleontologists 26, 1–144.

947 Meissner, P., Mutterlose, J., Bodin, S., 2015. Latitudinal temperature trends in the northern  
948 hemisphere during the Early Cretaceous (Valanginian-Hauterivian). *Palaeogeography,*  
949 *Palaeoclimatology, Palaeoecology* 424, 17–39.

950 Morales, C., Kujau, A., Heimhofer, U., Mutterlose, J., Spangenberg, J.E., Adatte, T., Ploch, I.,  
951 Föllmi, K.B., 2015. Palaeoclimate and palaeoenvironmental changes through the onset of the  
952 Valanginian carbon-isotope excursion: evidence from the Polish Basin. *Palaeogeography,*  
953 *Palaeoclimatology, Palaeoecology* 426, 183–198.

954 Morales, C., Rogov, M., Wierzbowski, H., Ershova, V., Suan, G., Adatte, T., Föllmi, K.B.,  
955 Tegelaar, E., Reichart, G.J., de Lange, G.J., Middelburg, J.J., van de Schootbrugge, B., 2017.  
956 Glendonites track methane seepage in Mesozoic polar seas. *Geology* 45, 503–506.

957 Melinte, M., Mutterlose, J., 2001. A Valanginian (Early Cretaceous) boreal nannoplankton  
958 excursion in sections from Romania. *Marine Micropaleontology* 43, 1–25.

959 Mutterlose, J., Malkoc, M., Schouten, S., Sinninghe Damsté, J.S., Forster, A., 2010. TEX<sub>86</sub> and  
960 stable  $\delta^{18}\text{O}$  paleothermometry of early Cretaceous sediments: Implications for belemnite  
961 ecology and paleotemperature proxy application. *Earth and Planetary Science Letters* 298,  
962 286–298.

963 Mutterlose, J., Malkoc, M., Schouten, S., Sinninghe Damsté, J.S., 2012. Reconstruction of vertical

964 temperature gradients in past oceans-Proxy data from the Hauterivian-early Barremian (Early  
965 Cretaceous) of the Boreal Realm. *Palaeogeography, Palaeoclimatology, Palaeoecology* 363-  
966 364, 135–143.

967 Ogg, J.G., Ogg, G., Gradstein, F.M., 2016. A concise Geologic Time Scale. Elsevier publication.  
968 240p.

969 Oglesby, R., Park, J., 1989. The effect of precessional insolation changes on Cretaceous climate and  
970 cyclic sedimentation. *Journal of Geophysical Research* 94, 14,793–14,816.

971 Pauly, S., Mutterlose, J., Alsen, P., 2012. Early Cretaceous palaeoceanography of the Greenland-  
972 Norwegian Seaway evidenced by calcareous nannofossils. *Marine Micropaleontology* 90-91,  
973 72–85.

974 Podlaha, O.G., Mutterlose, J., Veizer, J., 1998. Preservation of  $\delta^{18}\text{O}$  and  $\delta^{13}\text{C}$  in belemnite rostra  
975 from Jurassic/Early Cretaceous successions. *Am. J. Sci.* 298, 324–347.

976 Poulsen, C.J., Barron, E.J., Arthur, M.A., and Peterson, W.H., 2001, Response of the mid-  
977 Cretaceous global oceanic circulation to tectonic and  $\text{CO}_2$  forcings: *Paleoceanography* 16, 1–  
978 17.

979 Poulsen, C.J., Gendaszek, A.S., Jacob, R.L., 2003. Did the rifting of the Atlantic Ocean cause the  
980 Cretaceous thermal maximum? *Geology* 31, 115–118.

981 Price, G.D., 1999. The evidence and implications of polar ice during the Mesozoic. *Earth-Science*  
982 *Reviews* 48, 183–210.

983 Price, G.D., Mutterlose, J., 2004. Isotopic signals from late Jurassic-early Cretaceous (Volgian-  
984 Valanginian) sub-Arctic belemnites, Yatria River, Western Siberia. *Journal of the Geological*  
985 *Society London* 161, 959–968.

986 Price, G.D., Nunn, E.V., 2010. Valanginian isotope variation in glendonites and belemnites from  
987 Arctic Svalbard: transient glacial temperatures during the Cretaceous greenhouse. *Geology*  
988 38, 251–254.

989 Price, G.D., Passey, B.H., 2013. Dynamic polar climates in a greenhouse world: Evidence from

- 990 clumped isotope thermometry of Early Cretaceous belemnites. *Geology* 41, 923–926.
- 991 Price, G.D., Ruffell, A.H., Jones, C.E., Kalin, R.M., Mutterlose, J., 2000. Isotopic evidence for  
992 temperature variation during the Early Cretaceous. *Journal of Geological Society of London*  
993 157, 335–343.
- 994 Price, G.D., Wilkinson, D., Hart, M.B., Page, K.N., Grimes, S.T., 2009. Isotopic analysis of co  
995 existing late Jurassic fish otoliths and molluscs: implications for upper ocean water  
996 temperature estimates. *Geology* 37, 215–218.
- 997 Price, G.D., Williamson, T., Henderson, R.A., Gagan, M.K., 2012. Barremian–Cenomanian  
998 palaeotemperatures for Australian seas based on new oxygen-isotope data from belemnite  
999 rostra. *Palaeogeography, Palaeoclimatology, Palaeoecology* 358–360, 27–39.
- 1000 Price, G.D., Janssen, N.M.M., Martinez, M., Company, M., Vandeveld, J.H., Grimes, S.T., 2018.  
1001 A high-resolution belemnite geochemical analysis of Early Cretaceous (Valanginian-  
1002 Hauterivian) environmental and climatic perturbations. *Geochemistry, Geophysics,*  
1003 *Geosystems* 19.
- 1004 Pucéat, E., Lécuyer, C., Sheppard, S.M.F., Dromart, G., Reboulet, S., Grandjean, P., 2003. Thermal  
1005 evolution of Cretaceous Tethyan marine waters inferred from oxygen isotope composition of  
1006 fish tooth enamels. *Paleoceanography* 18, 1029–1041.
- 1007 Pucéat, E., Lécuyer, C., Reisberg, L., 2005. Neodymium isotope evolution of NW Tethyan upper  
1008 ocean waters throughout the Cretaceous. *Earth and Planetary Science Letter* 236, 705-720.
- 1009 Ray, D.C., van Buchem, F.S.P., Baines, G., Davies, A., Gréselle, B., Simmons, M.D., Robson, C.,  
1010 2019. The magnitude and cause of short-term eustatic Cretaceous sea-level change: A  
1011 synthesis. *Earth-Science Reviews* 197, 102901.
- 1012 Reinhardt, E.G., Cavazza, W., Patterson, R.T., Blenkinsop, J., 2000. Differential diagenesis of  
1013 sedimentary components and the implication for strontium isotope analysis of carbonate rocks.  
1014 *Chemical Geology* 164, 331–343.
- 1015 Reolid, M., Chakiri, S., Bejjaji, S., 2013. Adaptative strategies of the Toarcian benthic foraminiferal



- 1016 assemblages from the Middle Atlas (Morocco): Palaeoecological implications. *Journal of*  
1017 *African Earth Sciences* 84, 1–12.
- 1018 Ricken, W., 1986. Diagenetic Bedding: A Model for Limestone–marl Alternations. *Lecture Notes*  
1019 *in Earth Sciences* 6, Springer-Verlag, Berlin, 210 p.
- 1020 Ricken, W., 1987. The carbonate compaction law: a new tool. *Sedimentology* 34, 1–14.
- 1021 Robert, C., Maillot, H., 1990. Paleoenvironments in the Weddell Sea area and Antarctic climates, as  
1022 deduced from clay mineral associations and geochemical data, ODP Leg 113. *Proceedings of*  
1023 *the Ocean Drilling Program, Scientific Results, Vol. 113.*
- 1024 Sahagian, D., Pinous, O., Olferiev, A., Zakharov, V., 1996. Eustatic curve for the middle Jurassic–  
1025 Cretaceous based on Russian platform and Siberian stratigraphy: zonal re-resolution. *AAPG Bull.*  
1026 80, 1433–1458. <sup>[1]</sup><sub>SEP</sub>
- 1027 Scotese, C. R., 2001. *Atlas of Earth History, Volume 1, Paleogeography, PALEOMAP Project,*  
1028 *Arlington, Texas, 52 pp.*
- 1029 Schlager, W., 1989. Drowning unconformities on carbonate platforms. *SEPM Spec. Publ.* 44, 15–  
1030 25.
- 1031 Schouten, S., Hopmans, E.C., Forster, A., Breugel, van, Y., Kuypers, M.M.M., Sinninghe Damsté,  
1032 J.S., 2003. Extremely high sea-surface temperatures at low latitudes during the middle  
1033 Cretaceous as revealed by archaeal membrane lipids. *Geology* 31, 1069–1072.
- 1034 Sluijs, A., Schouten, S., Pagani, M., Woltering, M., Brinkhuis, H., Sinninghe Damsté, J.S., Dickens,  
1035 G.R., Huber, M., Reichert, G.-J., Stein, R., Matthiessen, J., Lourens, L.J., Pedentchouk, N.,  
1036 Backman, J., Moran, K., The Expedition 302 Scientists, 2006. Subtropical Arctic Ocean  
1037 temperatures during the Palaeocene–Eocene thermal maximum. *Nature* 441, 610–613.
- 1038 Sprovieri, M., Coccioni, R., Lirer, F., Pelosi, N., Lozar, F., 2006. Orbital tuning of a Lower  
1039 Cretaceous composite record (Maiolica Formation, central Italy). *Paleoceanography* 21,  
1040 PA4212.
- 1041 Stein, M., Föllmi, K.B., Westermann, S., Godet, A., Adatte, T., Matera, V., Fleitmann, D., Berner,

1042 Z., 2011. Progressive palaeoenvironmental change during the Late Barremian–Early Aptian as  
1043 prelude to Oceanic Anoxic Event 1a: evidence from the Gorgo a Cerbara section (Umbria-  
1044 Marche Basin, central Italy). *Palaeogeography, Palaeoclimatology, Palaeoecology* 302, 396–  
1045 406.

1046 Šucha, V., Kraust, I., Gerthofferova, H., Peteš, J., Serekova, M., 1993. Smectite to illite conversion  
1047 in bentonites and shales of the East Slovak Basin. *Clay Minerals* 28(2), 243-253.

1048 Thiede, D.S., and Vasconcelos, P.M., 2010, Parana flood basalts: rapid extrusion hypothesis  
1049 confirmed by new  $^{40}\text{Ar}/^{39}\text{Ar}$  results: *Geology*, v. 38, p. 747–750.

1050 Thiry, M., 2000. Palaeoclimatic interpretation of clay minerals in marine deposits: an outlook from  
1051 the continental origin. *Earth-Sci. Rev.* 49, 201–221.

1052 Tosolini, A.M.P., McLoughlin, S., Wagstaff, B.E., Cantrill, D.J., Gallagher, S.J., 2014.  
1053 Cheirolepidiacean foliage and pollen from Cretaceous high-latitudes of southeastern  
1054 Australia. *Gondwana Research* 27, 960-977.

1055 Upchurch Jr., G.R., Otto-Bliesner, B.L., Scotese, C., 1998. Vegetation-atmosphere interactions and  
1056 their role in global warming during the latest Cretaceous. *Philos. T. Roy. Soc. B* 353, 97–112.

1057 van de Schootbrugge, B., Föllmi, K., Bulot, L.G., Burns, S.J., 2000. Paleooceanographic changes  
1058 during the early Cretaceous (Valanginian–Hauterivian): evidence from oxygen and carbon  
1059 stable isotopes. *Earth and Planetary Science Letters* 181, 15–31.

1060 Veizer, J., 1983. Trace elements and isotopes in sedimentary carbonates. *Reviews in Mineralogy*  
1061 *and Geochemistry* 11, 265–299.

1062 Vickers, M.L., Price, G.D., Jerrett, R.M., Sutton, P., Watkinson, M.P., FitzPatrick, M., 2019. The  
1063 duration and magnitude of Cretaceous cool events: Evidence from the northern high latitudes.  
1064 *Geological Society of America Bulletin* 1-16 Inpress.

1065 Wagreich, M., Lein, R., Sames, B., 2014. Eustasy, its controlling factors, and the limno-eustatic  
1066 hypothesis concepts inspired by Eduard Suess. *Austrian Journal of Earth Sciences* 107, 115-  
1067 131.

- 1068 Weissert, H., 1989. C-isotope stratigraphy, a monitor of palaeoenvironmental change: a case study  
1069 from the early Cretaceous. *Surveys in Geophysics* 10, 1–61.
- 1070 Weissert, H., Erba, E., 2004. Volcanism, CO<sub>2</sub> and palaeoclimate: a Late Jurassic-Early Cretaceous  
1071 carbon and oxygen isotope record. *Journal of the Geological Society, London* 161, 1–8.
- 1072 Weissert, H., Lini, A., Föllmi, K. B., Kuhn, O., 1998. Correlation of Early Cretaceous carbon  
1073 isotope stratigraphy and platform drowning events: a possible link? *Palaeogeography,*  
1074 *Palaeoclimatology, Palaeoecology* 137, 189–203.
- 1075 Wendler, I., 2013. A critical evaluation of carbon isotope stratigraphy and biostratigraphic  
1076 implications for Late Cretaceous global correlation. *Earth Science Reviews* 126, 116–146.
- 1077 Wendler, J.E., Wendler, I., Vogt, C., Kuss, J., 2016. Link between cyclic eustatic sea-level change  
1078 and continental weathering: Evidence for aquifer-eustasy in the Cretaceous. *Palaeogeography,*  
1079 *Palaeoclimatology, Palaeoecology* 441, 430-437.
- 1080 Westermann, S., Duchamp-Alphonse, S., Fiet, N., Fleitmann, D., Matera, V., Adatte, T., and  
1081 Föllmi, K.B., 2013, Paleoenvironmental changes during the Valanginian: new insights from  
1082 variations in phosphorus contents and bulk- and clay mineralogies in the western Tethys:  
1083 *Palaeogeography, Palaeoclimatology, Palaeoecology*, 392, 196–208.
- 1084 Westermann, S., Föllmi, K.B., Adatte, T., Matera, V., Schnyder, J., Fleitmann, D., Fiet, N., Ploch,  
1085 I., Duchamp-Alphonse, S., 2010. The Valanginian  $\delta^{13}\text{C}$  excursion may not be an expression  
1086 of a global anoxic event. *Earth Planetary Science Letter* 290, 118-131.
- 1087 Westphal, H., Head, M.J., Munnecke, A., 2000. Differential diagenesis of rhythmic limestone  
1088 alternations supported by palynological evidence. *Journal of Sedimentary Research* 70, 715–  
1089 725.
- 1090 Westphal, H., Munnecke, A., Böhm, F., Bornholdt, S., 2008. Limestone-marl alternations in  
1091 epeiric sea settings—witnesses of environmental changes, or of rhythmic diagenesis?  
1092 *Geological Association of Canada Special Paper* 48, 389–406.
- 1093 Wierzbowski, H., 2002. Detailed oxygen and carbon isotope stratigraphy of the Oxfordian in

1094 Central Poland. *International Journal of Earth Sciences* 91, 304–314.

1095 Zemmels, I., Cook, H.E., Hathaway, J.C., 1972. X-Ray mineralogy studies Leg 11. The Shipboard  
1096 Scientific party.

1097 Ziegler, A.M., Raymond, A.L., Gierlowski, T.C., Horrell, M.A., Rowley, D.B., Lottes, A.L., 1987.  
1098 Coal, climate and terrestrial productivity: the present and the early Cretaceous compared.  
1099 Geological Society Special Publication 32, 22–49.

1100 Zhou, J., Poulsen, C.J., Pollard, D., White, T.S., 2008. Simulation of modern and middle Cretaceous  
1101 marine  $\delta^{18}\text{O}$  with an ocean–atmosphere general circulation model. *Paleoceanography* 23,  
1102 PA3223.

## 1104 **Figure captions**

1105  
1106 **Fig. 1:** World palaeogeographic map of the Early Cretaceous (modified after Blakey, 2010).  
1107 Locations of the studied sections in four depositional environments at several palaeolatitudes (see  
1108 Table 1): (1) Wawal core (Polish Basin), (2) Angles section (Vocontian Basin), (3) Orpierre section  
1109 (Vocontian Basin), (4) Barranco del Garranchal section (Subbetic Basin), (5) Molina de las Oicas  
1110 section (Subbetic Basin), (6) DSDP Hole 603B (Continental rise Cape Hatteras), (7) DSDP Hole  
1111 534A (Blake Bahama Basin), (8) DSDP Hole 535 (Gulf of Mexico), (9) ODP Hole 765C (Argo  
1112 abyssal plain), (10) Speeton section (Yorkshire), (11) Northwest Germany composite section  
1113 (Lower Saxony Basin), (12) Northern Germany composite section (Proto-North Sea Basin), (13)  
1114 Vergol/La Charce sections (Vocontian Basin), (14) Vocontian composite section (Vocontian Basin),  
1115 (15) Subbetic composite section (Subbetic Basin), (16) Umbria Marche composite section (Umbria  
1116 Marche Basin), (17) Bersek Quarry (Gerecse Mountains), (18) Kozoskut ravine section (Bakony  
1117 Mountains), (19) Cehegín section (southern Iberian continental margin) (20) ODP Hole 766A  
1118 (Gascoyne and Cuvier abyssals plains).

1119  
1120 **Fig. 2:** Synthesis diagram showing kaolinite, smectite,  $\delta^{18}\text{O}_{\text{carb}}$  and  $\delta^{18}\text{O}_{\text{bel}}$  LOESS smoothing

1121 curves from the northwestern Tethyan realm with the carbon isotope stratigraphy against the  
1122 biostratigraphic scheme. LOESS, i.e. locally weighted scatterplot smoothing (Cleveland and Devlin,  
1123 1988). For the calculation of LOESS smoothing curve (red line) an  $\alpha$  value of 0.15 has been  
1124 applied. Blue curves indicate the 95 % confidence interval. SST: Sea Surface Temperature, SWT:  
1125 Sea Water Temperature.

1126

1127 **Fig. 3:** Synthesis diagram showing kaolinite, smectite,  $\delta^{18}\text{O}_{\text{carb}}$  and  $\text{TEX}_{86}$  LOESS smoothing  
1128 curves from the Proto North Atlantic realm with the carbon isotope stratigraphy against the  
1129 biostratigraphic scheme. LOESS, i.e. locally weighted scatterplot smoothing (Cleveland and Devlin,  
1130 1988). For the calculation of LOESS smoothing curve (red line) an  $\alpha$  value of 0.15 has been  
1131 applied. Blue curves indicate the 95 % confidence interval. SST: Sea Surface Temperature.

1132

1133 **Fig. 4:** Synthesis diagram showing kaolinite, smectite,  $\delta^{18}\text{O}_{\text{lent}}$  and  $\delta^{18}\text{O}_{\text{bel}}$  LOESS smoothing curves  
1134 from the southern Boreal realm with the carbon isotope stratigraphy against the biostratigraphic  
1135 scheme. LOESS, i.e. locally weighted scatterplot smoothing (Cleveland and Devlin, 1988). For the  
1136 calculation of LOESS smoothing curve (red line) an  $\alpha$  value of 0.15 has been applied. Blue curves  
1137 indicate the 95 % confidence interval. SST: Sea Surface Temperature, SWT: Sea Water  
1138 Temperature.

1139

1140 **Fig. 5:** Synthesis diagram showing kaolinite, smectite,  $\delta^{18}\text{O}_{\text{carb}}$  and  $\text{TEX}_{86}$  LOESS smoothing  
1141 curves from the southern Tethyan realm with the carbon isotope stratigraphy against the  
1142 biostratigraphic scheme. LOESS, i.e. locally weighted scatterplot smoothing (Cleveland and Devlin,  
1143 1988). For the calculation of LOESS smoothing curve (red line) an  $\alpha$  value of 0.15 has been  
1144 applied. Blue curves indicate the 95 % confidence interval. SST: Sea Surface Temperature.

1145

1146 **Fig. 6:** Cross-plot of the  $\delta^{13}\text{C}_{\text{carb}}$  and the  $\delta^{18}\text{O}_{\text{carb}}$  values from the northwestern Tethyan, Proto North  
1147 Atlantic and southern Tethyan realms.

1148

1149 **Fig. 7:** Evolution of kaolinite contents and temperature ranges during (i) the early Valanginian, (ii)  
1150 the early-late Valanginian transition, and (iii) the late Valanginian. Palaeogeographic map are from  
1151 Blakey (2010).

1152

1153 **Fig. 8:** Synthetic map (modified after Blakey, 2010) illustrating the Valanginian palaeoclimatic  
1154 belts supported by geochemical and mineralogical data during the early Valanginian, the early-late  
1155 Valanginian transition, and the late Valanginian. Location of Berriasian, Valanginian and  
1156 Hauterivian coal deposits are reported after McCabe and Totman-Parrish (1992). Distribution of  
1157 conifer forest are from Dettmann et al. (1992); McLoughlin and Hill (1996); McLoughlin et al.  
1158 (2002); Galloway et al. (2013, 2015); and Tosolini et al. (2014). Distribution of glendonites,  
1159 dropstones and tillites are from Kemper and Schmitz (1975), Kemper (1987), Price (1999), Alley  
1160 and Frakes (2003), Price and Nunn (2010), and Alley et al. (2019). Reconstruction of the  
1161 palaeoclimatic belts that prevailed during the Berriasian (modified after Chumakov et al., 1995).

1162

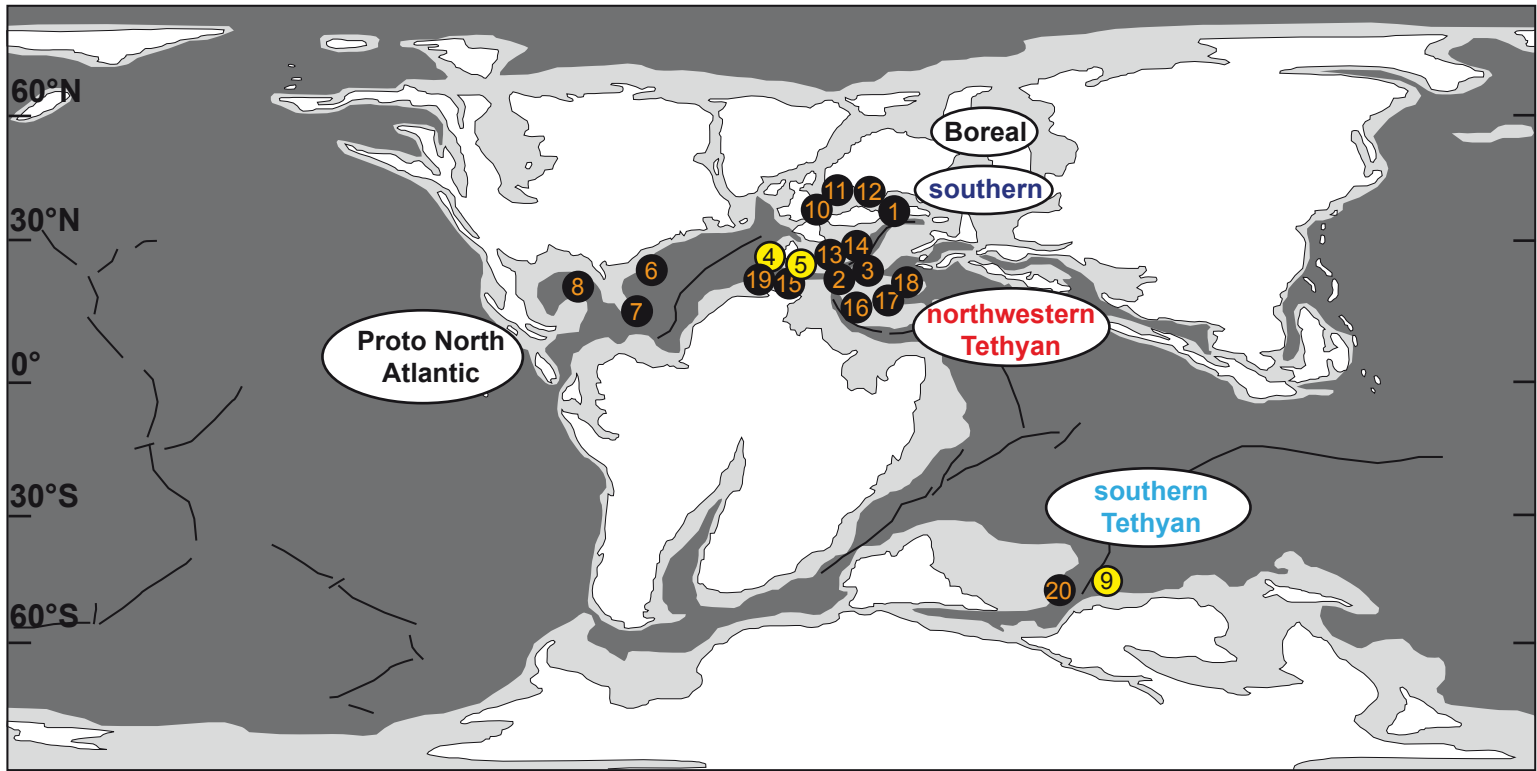
### 1163 **Table captions**

1164

1165 **Table 1:** Mineralogical, and geochemical data set compilation.

1166

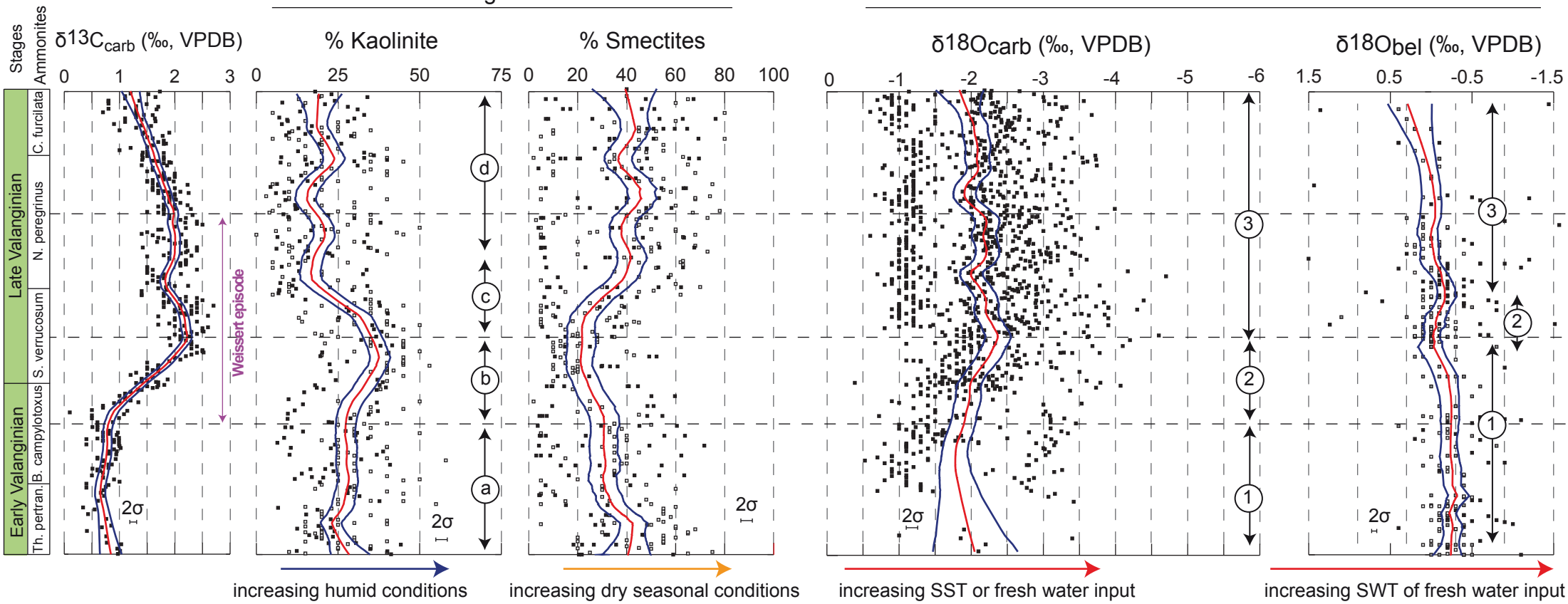
1167 **Table 2:** Seawater palaeotemperatures calculation applying the equation of Anderson and Arthur  
1168 (1983) and using various  $\delta^{18}\text{O}_w$  values according to the latitude (Zhou et al., 2008; Price et al.,  
1169 2018).



## Northwestern Tethyan realm (~20-30°N)

### Mineralogical data

### Geochemical data



#### Mineralogical and geochemical data references:

**Clay mineralogy data:**

- Duchamp-Alphonse et al., 2011; Charbonnier et al., 2016
- This Study

**$\delta^{13}\text{C}_{\text{carb}}$  data:** Duchamp-Alphonse et al., 2007; Kujau et al., 2012

**$\delta^{18}\text{O}_{\text{carb}}$  data:** Sprovieri et al., 2006; Duchamp-Alphonse et al., 2007; Fozy et al., 2010; Gréselle et al., 2011; Kujau et al., 2012; Charbonnier et al., 2016; Bajnai et al., 2017; Aguado et al., 2018

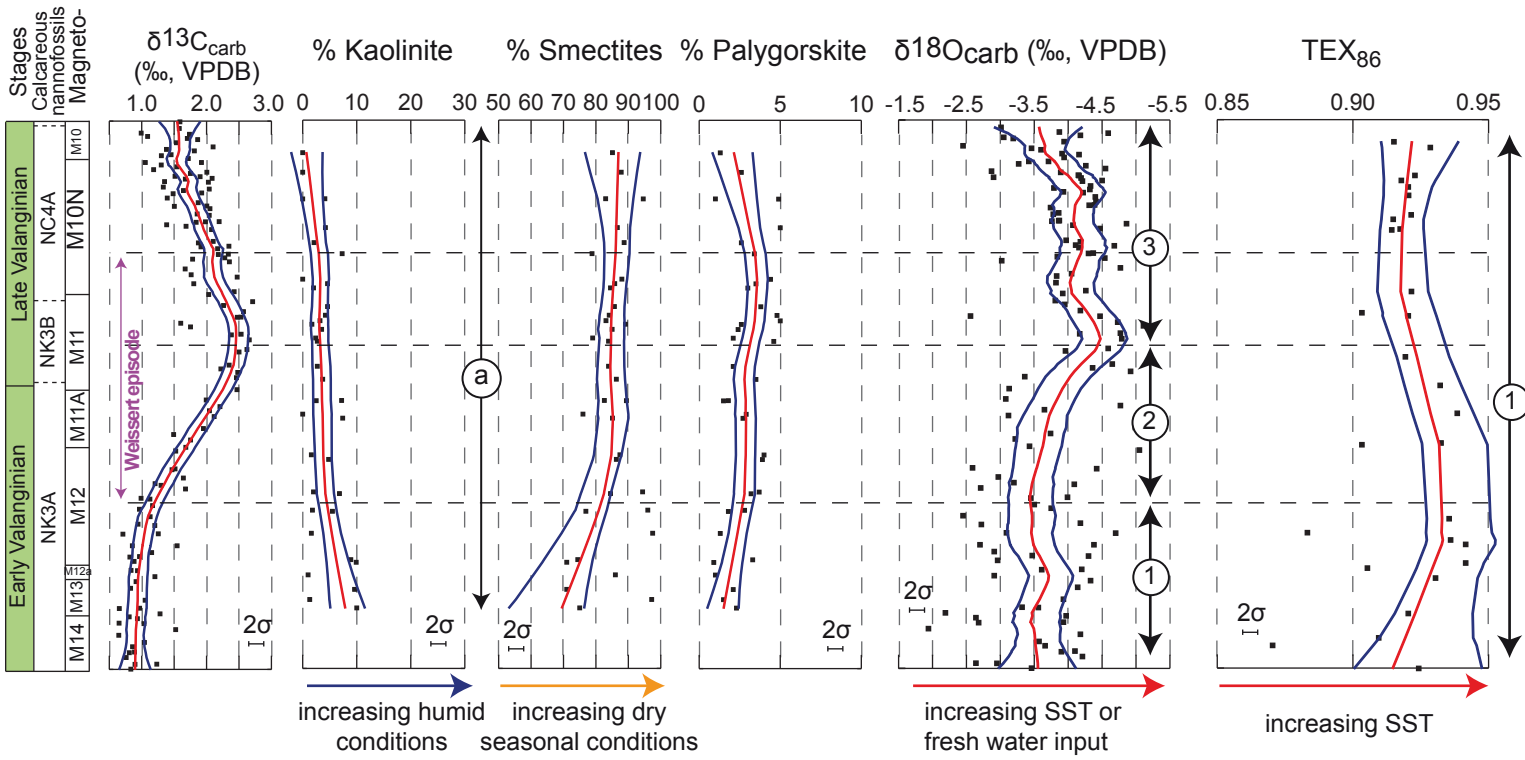
**$\delta^{18}\text{O}_{\text{bel}}$  data:** van de Schootbrugge et al., 2000; McArthur et al., 2007; Price et al., 2018



# Proto North Atlantic realm (~15-17°N)

## Mineralogical data

## Geochemical data



### Mineralogical and geochemical data references:

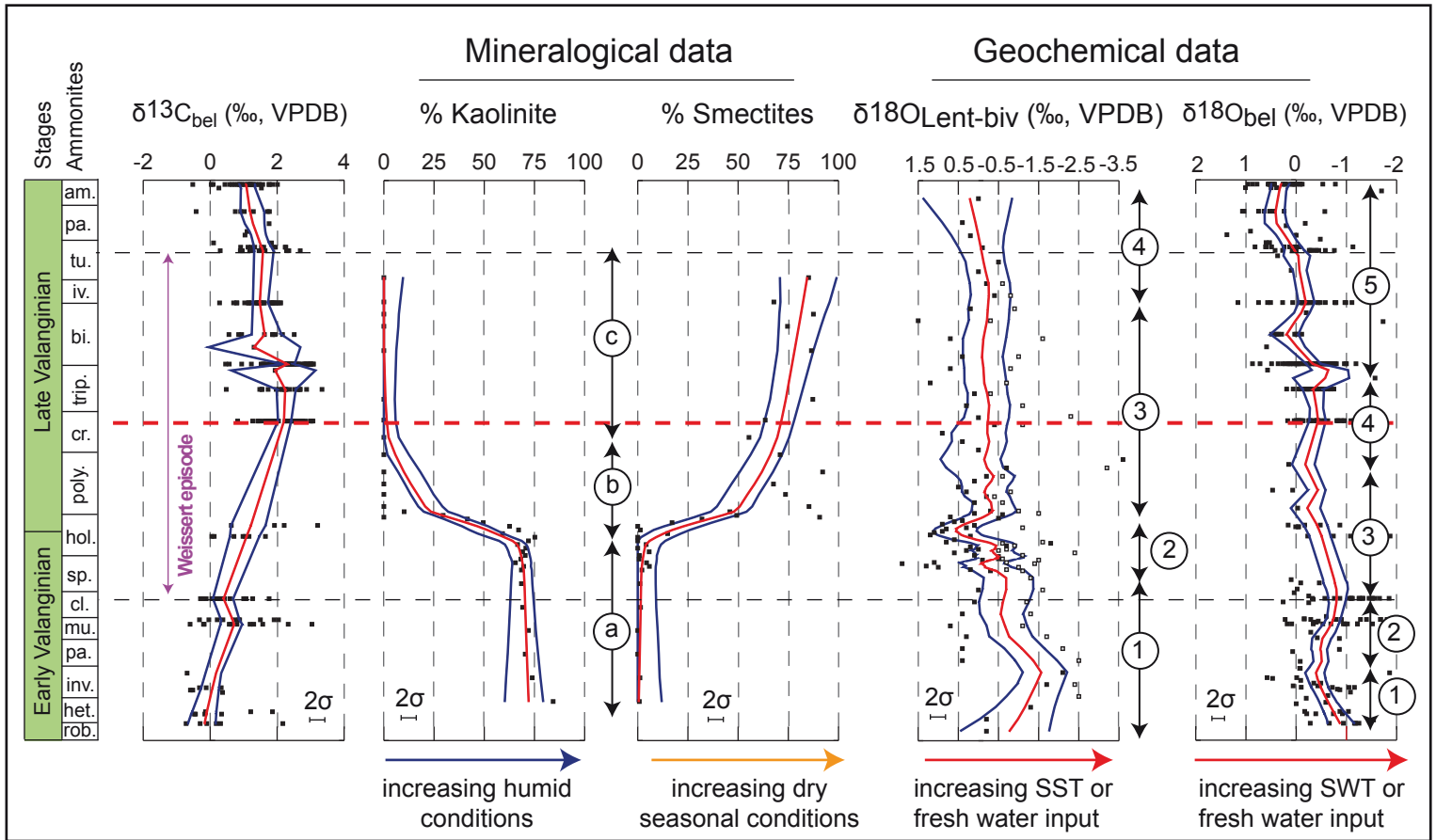
**Clay mineralogy data:** Chamley et al., 1983; Debrabant et al., 1984; Huff, 1993

**$\delta^{13}\text{C}_{\text{carb}}$  data:** Bornemann and Mutterlose, 2008

**$\delta^{18}\text{O}_{\text{carb}}$  data:** Bornemann and Mutterlose, 2008

**TEX<sub>86</sub> data:** Littler et al., 2011

southern part of the Boreal realm (~35-45°N)



Mineralogical and geochemical data references:

$\delta^{13}C_{carb}$  data: Meissner et al., 2015

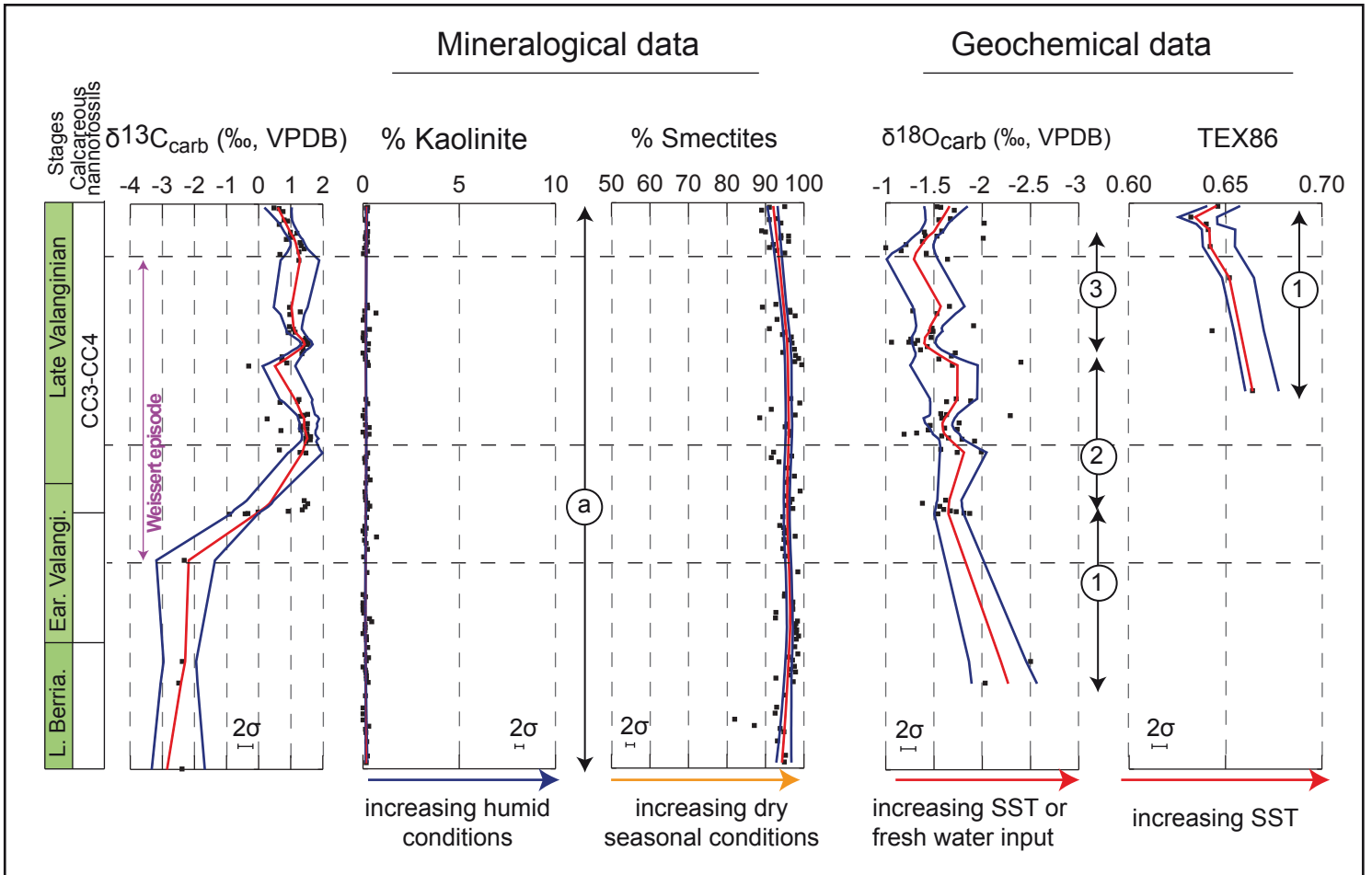
Clay mineralogy data: Morales et al., 2015

$\delta^{18}O_{biv}$  data ■ Morales et al., 2015

$\delta^{18}O_{Lent}$  data □

$\delta^{18}O_{bel}$  data: Podlaha et al., 1998; Price et al., 2000; McArthur et al., 2004; Meissner et al., 2015

# southern Tethyan realm (~53°S)



Mineralogical and geochemical data references:

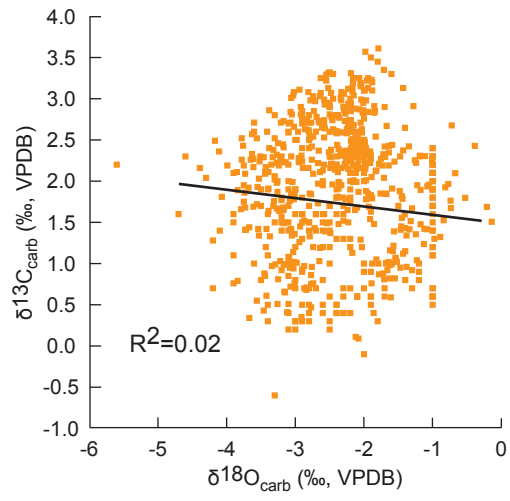
$\delta^{13}\text{C}_{\text{carb}}$  data: Charbonnier et al., 2020

Clay mineralogy data: This Study

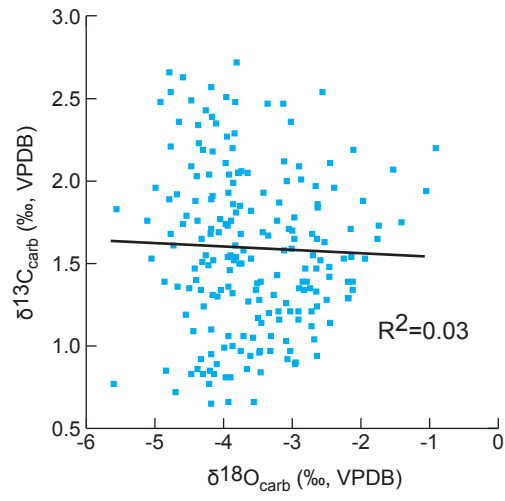
$\delta^{18}\text{O}_{\text{carb}}$  data: This Study

TEX<sub>86</sub> data: Littler et al., 2011

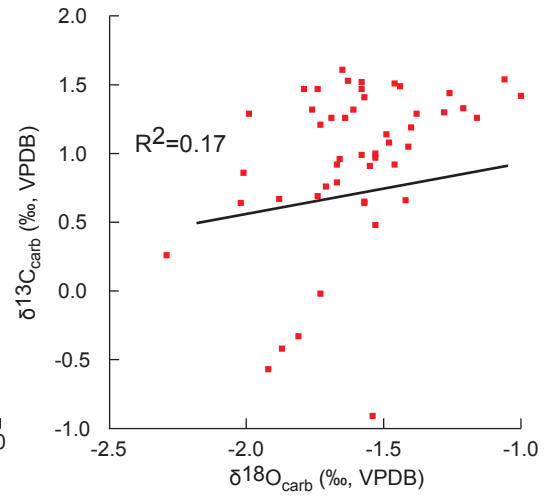
Northwestern Tethyan



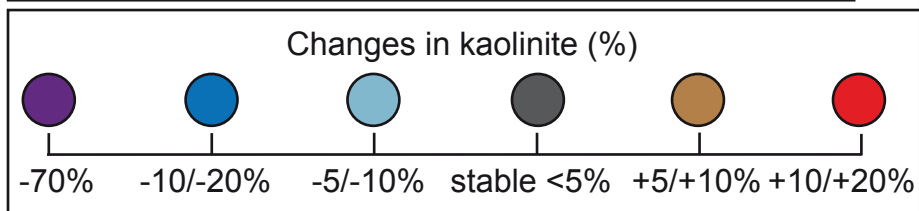
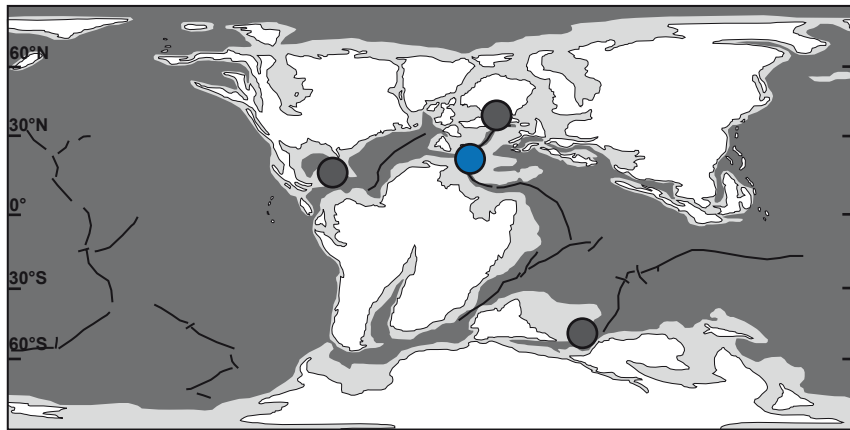
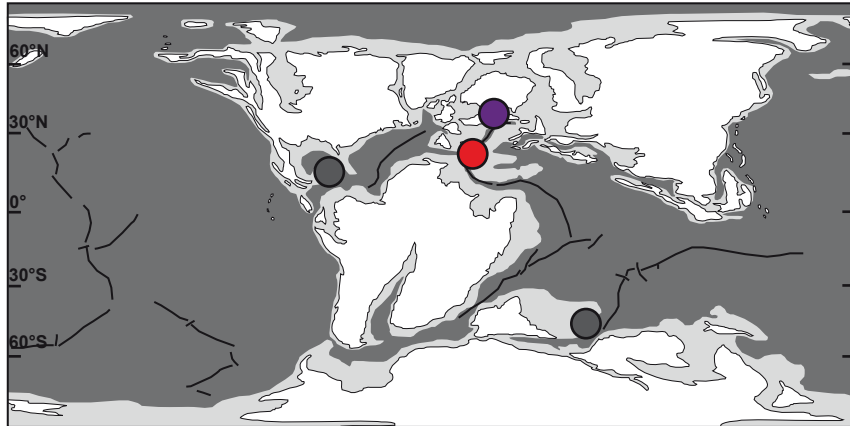
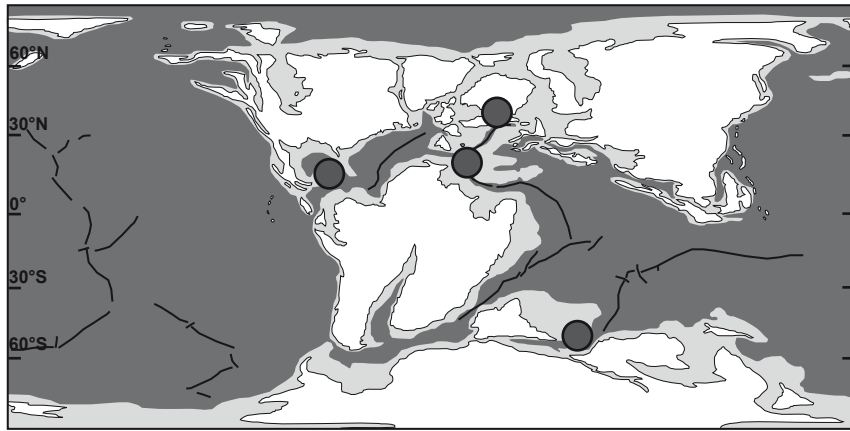
Proto North Atlantic



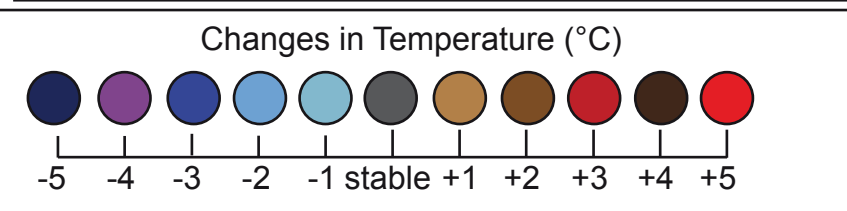
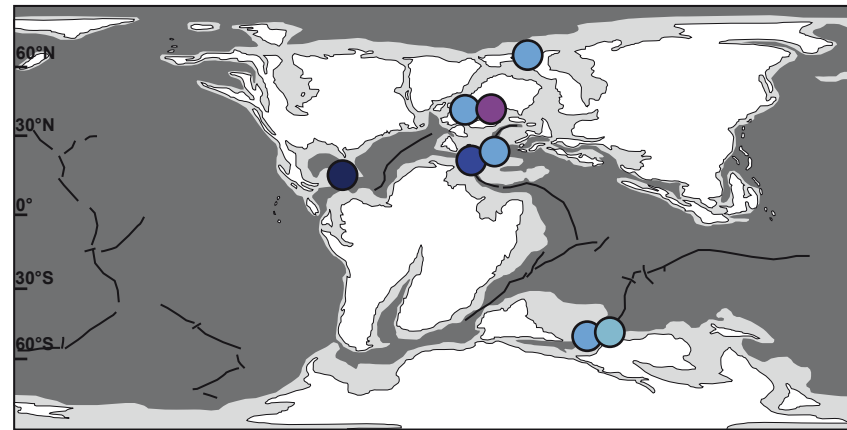
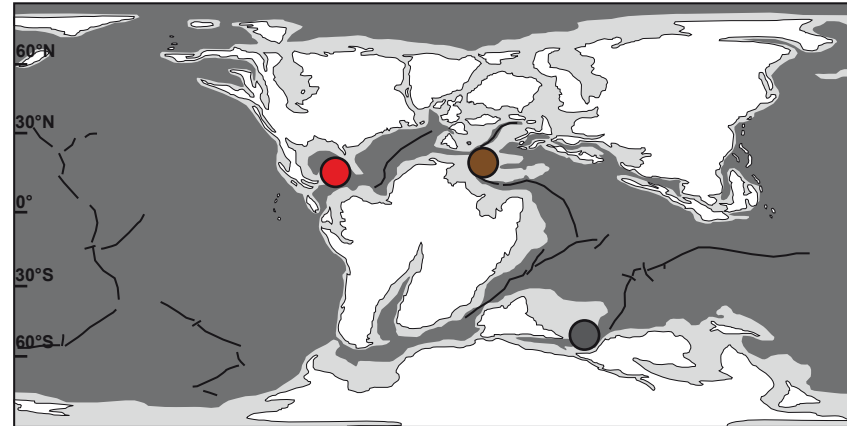
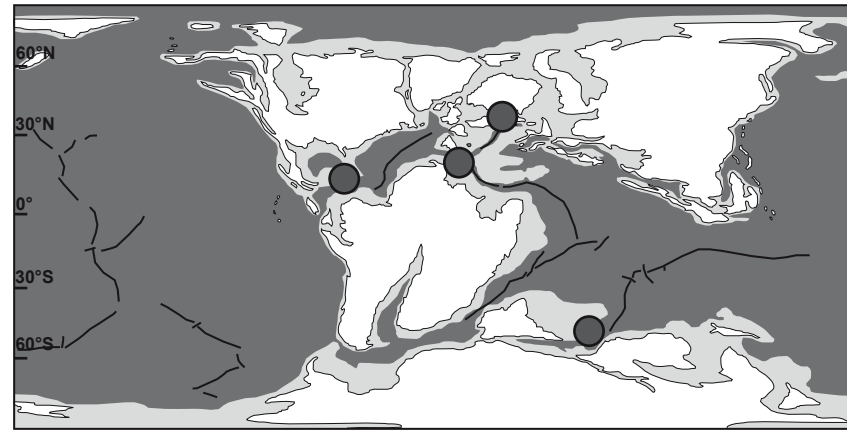
Southern Tethyan



## Clay mineralogy assemblages



## Temperatures



### early Valanginian:

*T. pertransiens*  
*B. campylotoxus*

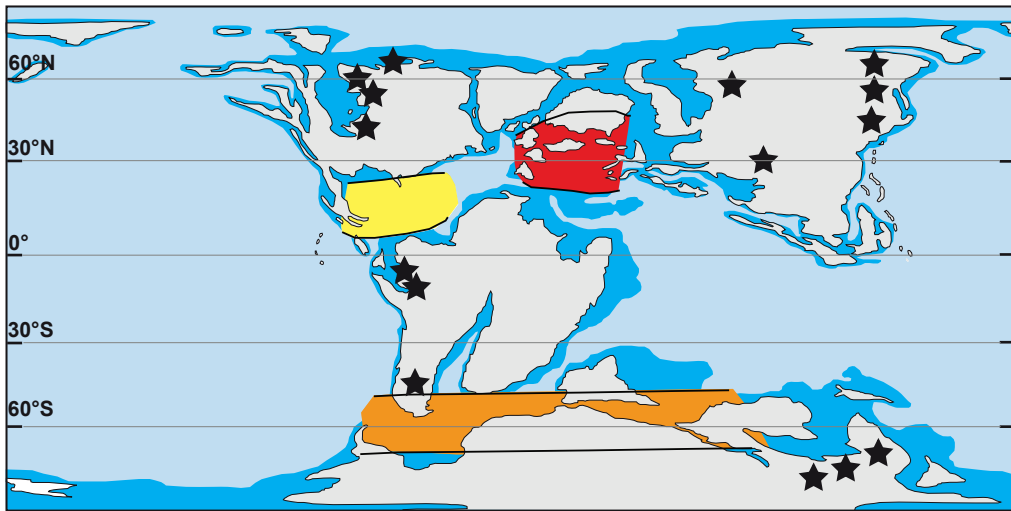
### early-late Valanginian transition:

*B. campylotoxus*-*S. verrucosum* transition

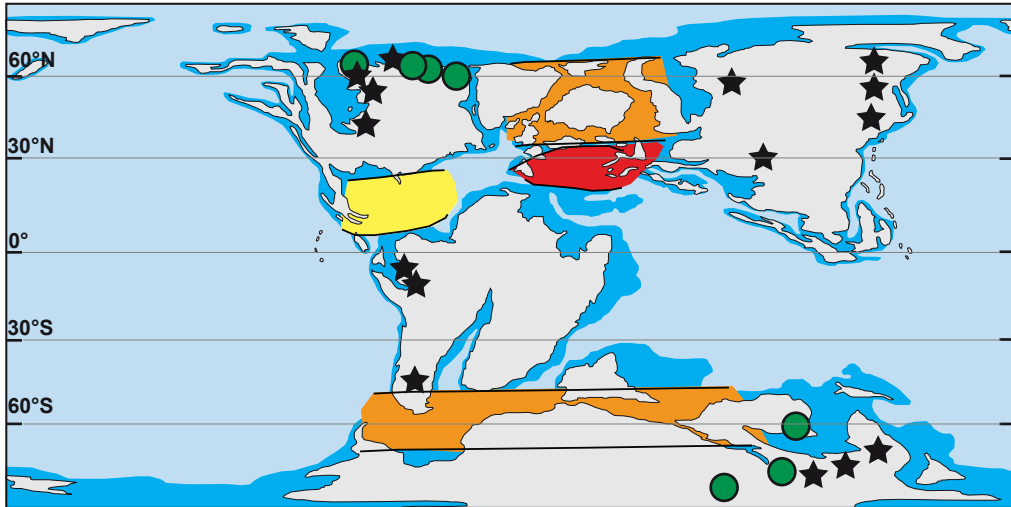
### late Valanginian:

upper part *S. verrucosum*  
*N. peregrinus*  
*C. furcilitata*

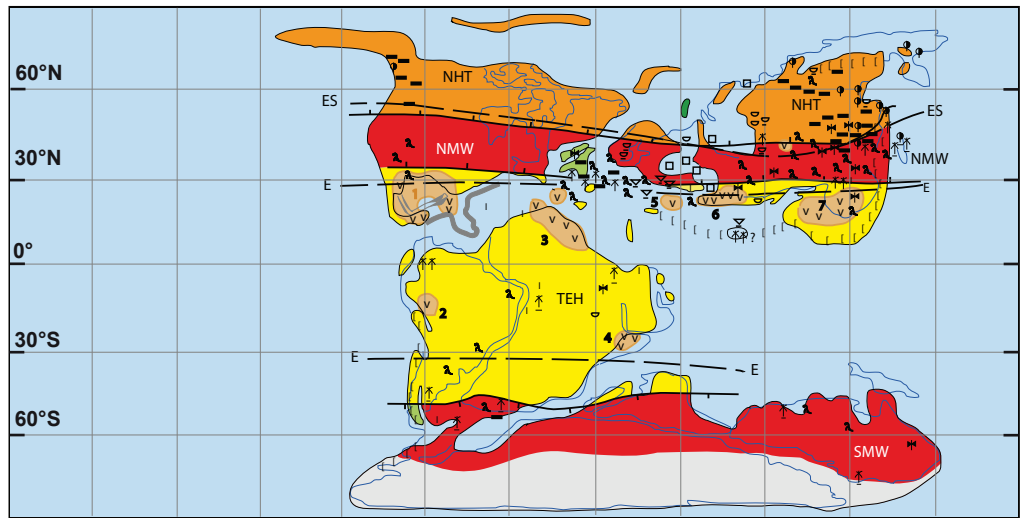
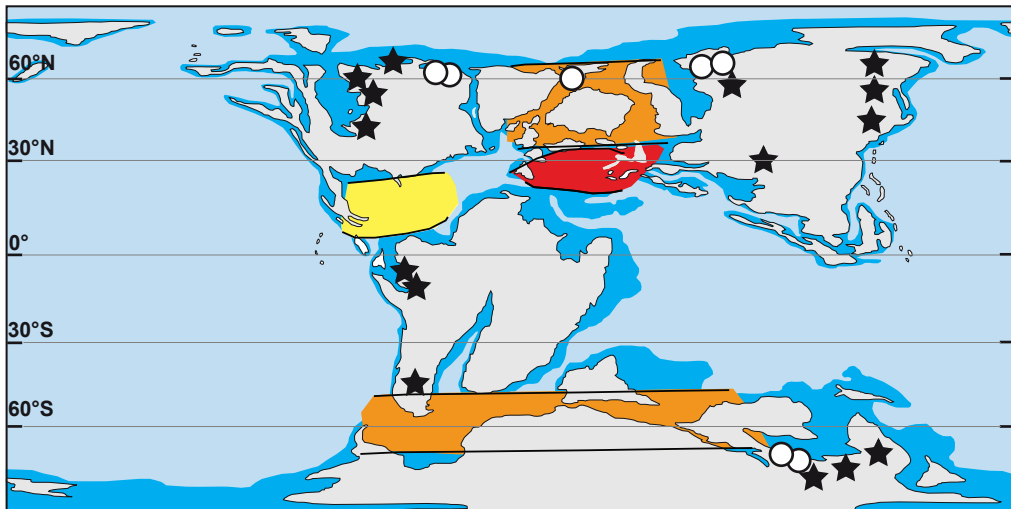
early Valanginian









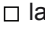

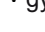


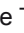


early-late Valanginian transition






late Valanginian





	high-latitude temperate belts		moderately thermophilic vegetation
	mid-latitude warm humid belts		moderately thermophilic insects
	evaporite belts		thermophilic insects
	arid belts		thermophilic vegetation
	laterite and clastic iron ores of terrestrial origin		localities of dinosaur remains
	gypsum and anhydrite deposits		coal and lignite deposits
			sedimentary and laterite bauxites
			kaolin weathering crusts or deposits

NHT: Northern High-latitude Temperate humid belt  
 SHT: Southern High-latitude Temperate humid belt  
 NMW: Northern Mid-latitude Warm humid belt  
 SMW: Southern Mid-latitude Warm humid belt  
 TEH: Tropical -Equatorial Hot arid belt  
 NHA: Northern Hot Arid belt  
 EH: Equatorial Humid belt  
 SHA: Southern Hot Arid belt

Valanginian latitudinal belts:

	sub-arid belt		humid subtropical belt
	Warm temperate belt		

Vegetation cover:

	Distribution of conifer forests		Location of Berriasian-Valanginian-Hauterivian coal deposits
---	---------------------------------	---	--

Ice rafted indicator:


	Distribution of dropstones/glendonites/tillites
---	---

Table 1: Mineralogical, and geochemical data set compilation

## A) Mineralogical data

Section	Basin	N° section Fig. 1	Latitude	Depositional environment	Realm	lithology	Analyses	References
Wawal core	Polish Basin	1	35-40°N	proximal setting	Southern part of the Boreal	sandy and silty claystone	clay <2µm fraction	Morales et al., 2015
Angles	Vocontian Basin	2	25-30°N	hemipelagic setting	northwestern Tethyan	marl-limestone alternations	clay <2µm fraction	Duchamp-Alphonse et al., 2011
Orpierre	Vocontian Basin	3	25-30°N	hemipelagic setting	northwestern Tethyan	marl-limestone alternations	clay <2µm fraction	Charbonnier et al., 2016
Barranco del Garranchal	Subbetic Basin	4	20-30°N	hemipelagic setting	northwestern Tethyan	marl-limestone alternations	clay <2µm fraction	This study
Molina de las Oicas	Subbetic Basin	5	20-30°N	hemipelagic setting	northwestern Tethyan	marl-limestone alternations	clay <2µm fraction	This study
Site 603B	Continental rise Cape Hatteras	6	~17°N	pelagic setting	proto North Atlantic	laminated and bioturbated pelagic limestones	clay <2µm fraction	Huff, 1993
Site 534A	Blake Bahama Basin	7	~15°N	pelagic setting	proto North Atlantic	laminated and bioturbated pelagic carbonates	clay <2µm fraction	Chamley et al., 1983
Site 535	Gulf of Mexico	8	~15°N	pelagic setting	proto North Atlantic	limestone and marly limestone	clay <2µm fraction	Debrabant et al., 1984
Site 765C	Argo abyssal plain	9	~53°S	abyssal plain	southern Tethyan	pelagic claystone and nannofossil chalk	clay <2µm fraction	This study

## B) Geochemical data

Section	Basin	N° section Fig. 1	Latitude	Depositional environment	Location	lithology	Analyses	References
Speeton	Yorkshire	10	~40-45°N	epicontinental sea	Southern part of the Boreal	clay formation, calcareous mudrocks	belemnites	Price et al., 2000; McArthur et al., 2004
Northwest Germany	Lower Saxony Basin	11	~38-42°N	epicontinental sea	Southern part of the Boreal	mudstones with slightly silty	belemnites	Meissner et al., 2015
Northern Germany	Proto-North Sea Basin	12	38°N	shallow marin	Southern part of the Boreal	terrigeneous brackish	belemnites	Podlaha et al., 1998
Wawal core	Polish Basin	1	35-40°N	proximal setting	Southern part of the Boreal	sandy and silty claystone	whole rock	Morales et al., 2015
Angles	Vocontian Basin	2	25-30°N	hemipelagic setting	northwestern Tethyan	marl-limestone alternations	whole rock	Duchamp-Alphonse et al., 2007
Orpierre	Vocontian Basin	3	25-30°N	hemipelagic setting	northwestern Tethyan	marl-limestone alternations	whole rock	Charbonnier et al., 2016
Vergol/La Charce	Vocontian Basin	13	25-30°N	hemipelagic setting	northwestern Tethyan	marl-limestone alternations	whole rock	Gréselle et al., 2011; Kujau et al., 2012
Composite section	Vocontian Basin	14	25-30°N	hemipelagic setting	northwestern Tethyan	marl-limestone alternations	belemnites	van de Schootbrugge et al., 2000; McArthur et al., 2007. Price et al., 2018
Composite section	Subbetic Basin	15	20-30°N	hemipelagic setting	northwestern Tethyan	marl-limestone alternations	belemnites	Price et al., 2018
Composite section	Umbria Marche Basin	16	~20°N	pelagic setting	northwestern Tethyan	white to gray pelagic limestone	whole rock	Sprovieri et al., 2006
Bersek quarry	Gerecse Mountains	17	~20°N	foreland basin	northwestern Tethyan	Grey-purple marlstone	whole rock	Bajnai et al., 2017
Kozoskut ravine	Bakony Mountains	18	~20°N	pelagic setting	northwestern Tethyan	Cherty marls and limestone	whole rock	Fozy et al., 2010
Cehegin	South Iberian Continental margin	19	~25°N	hemipelagic setting	northwestern Tethyan	marl-limestone alternations	whole rock	Aguado et al., 2018
Site 603B	Continental rise Cape Hatteras	6	~17°N	pelagic setting	proto North Atlantic	laminated and bioturbated pelagic limestones	TEX86, SSTs	Littler et al., 2011
Site 603B	Continental rise Cape Hatteras	6	~17°N	pelagic setting	proto North Atlantic	laminated and bioturbated pelagic limestones	whole rock	Bornemann and Mutterlose, 2008
Site 534A	Blake Bahama Basin	7	~15°N	pelagic setting	proto North Atlantic	laminated and bioturbated pelagic carbonates	TEX86, SSTs	Littler et al., 2011
Site 534A	Blake Bahama Basin	7	~15°N	pelagic setting	proto North Atlantic	laminated and bioturbated pelagic carbonates	whole rock	Bornemann and Mutterlose, 2008
Site 766A	Gascoyne and Cuvier abyssals plains	20	~53°S	abyssal plain	southern Tethyan	varicolored pelagic claystone and nannofossil chalk	TEX86, SSTs	Littler et al., 2011
Site 765C	Argo abyssal plain	9	~53°S	abyssal plain	southern Tethyan	pelagic claystone and nannofossil chalk	whole rock	This study

Table 2  
northwestern Tethyan realm

$\delta^{18}\text{O}_w$	$\delta^{18}\text{O}_{\text{calcite}}$			$\delta^{18}\text{O}_w$	$\delta^{18}\text{O}_{\text{calcite}}$		
	early-late Valanginian transition				late Valanginian		
	-1.87‰	-2.4‰	$\Delta T^\circ\text{C}$		-2.4‰	-1.8‰	$\Delta T^\circ\text{C}$
1.0‰	28.7°C	31.3°C	<b>2.6°C</b>	1.0‰	31.3°C	28.4°C	<b>2.9°C</b>
1.4‰	30.7°C	33.4°C	<b>2.7°C</b>	1.2‰	32.3°C	29.4°C	<b>2.9°C</b>
	average		<b>3°C</b>		average		<b>3°C</b>

Proto North Atlantic realm

$\delta^{18}\text{O}_w$	$\delta^{18}\text{O}_{\text{calcite}}$			$\delta^{18}\text{O}_w$	$\delta^{18}\text{O}_{\text{calcite}}$		
	early-late Valanginian transition				late Valanginian		
	-3.65‰	-4.5‰			-4.5‰	-3.62‰	$\Delta T^\circ\text{C}$
0.5‰	35.2°C	39.7°C	<b>4.5°C</b>	0.5‰	39.7°C	35.0°C	<b>4.7°C</b>
	average		<b>5°C</b>		average		<b>5°C</b>

southern part of the Boreal realm

$\delta^{18}\text{O}_w$	$\delta^{18}\text{O}_{\text{Lent+biv}}$		
	late Valanginian		
	-0.28‰	0.2‰	$\Delta T^\circ\text{C}$
0‰	17.0°C	15.0°C	<b>2.0°C</b>
-0.5‰	14.9°C	13.0°C	<b>1.9°C</b>
	average		<b>2°C</b>

Southern Tethyan realm

$\delta^{18}\text{O}_w$	$\delta^{18}\text{O}_{\text{calcite}}$		
	late Valanginian		
	-1.6‰	-1.3‰	$\Delta T^\circ\text{C}$
-1.5‰	16.6°C	15.0°C	<b>1.6°C</b>
	average		<b>2°C</b>